BIOPHYSICS

Noncanonical interaction with microtubules via the N-terminal nonmotor domain is critical for the functions of a bidirectional kinesin

Sudhir K. Singh[1]†‡, Nurit Siegler[1]†, Himanshu Pandey[1]†§, Neta Yanir[1], Mary Popov[1], Alina Goldstein-Levitin[1], Mayan Sadan[1], Garrett Debs[2], Raz Zarivach[3,4,5], Gabriel A. Frank[3,4,5], Itamar Kass[4], Charles V. Sindelar[2], Ran Zalk[4]*, Larisa Gheber[1,4]*

Several kinesin-5 motors (kinesin-5s) exhibit bidirectional motility. The mechanism of such motility remains unknown. Bidirectional kinesin-5s share a long N-terminal nonmotor domain (NTnmd), absent in exclusively plus-end–directed kinesins. Here, we combined in vivo, in vitro, and cryo–electron microscopy (cryo-EM) studies to examine the impact of NTnmd mutations on the motor functions of the bidirectional kinesin-5, Cin8. We found that NTnmd deletion mutants exhibited cell viability and spindle localization defects. Using cryo-EM, we examined the structure of a microtubule (MT)-bound motor domain of Cin8, containing part of its NTnmd. Modeling and molecular dynamic simulations based on the cryo-EM map suggested that the NTnmd of Cin8 interacts with the C-terminal tail of β-tubulin. In vitro experiments on subtilisin-treated MTs confirmed this notion. Last, we showed that NTnmd mutants are defective in plus-end–directed motility in single-molecule and antiparallel MT sliding assays. These findings demonstrate that the NTnmd, common to bidirectional kinesin-5s, is critical for their bidirectional motility and intracellular functions.

INTRODUCTION

Kinesin-5 motor proteins (kinesin-5s) are essential for mitotic chromosome segregation, facilitating mitotic spindle assembly, maintenance, and elongation [reviewed in (*1*–*4*)]. These proteins are bipolar kinesins, with two pairs of catalytic motor domains located on opposite sides of an elongated homotetrameric complex (*5*–*7*). By virtue of this bipolar structure, kinesin-5s cross-link the antiparallel microtubules (MTs) of the spindle, and by moving on the two cross-linked MTs, they provide the outwardly directed force essential for spindle pole separation during spindle assembly and anaphase B spindle elongation (*1*–*4*).

Within the mitotic spindle, the MTs are oriented with their dynamic plus-ends facing the middle of the spindle, while the less dynamic minus-ends are concentrated at the poles. It would seem that, as a result of this MT architecture, the function of kinesin-5s in separating the spindle poles could be achieved only via plus-end–directed motility on the two MTs that they cross-link (*1*–*4*). However, several studies have indicated that the fungal kinesin-5s, Cin8 and Kip1 from *Saccharomyces cerevisiae* and Cut7 from *Schizosaccharomyces pombe*, are bidirectional motors that can move in opposite directions on the MTs, depending on the experimental conditions (*8*–*11*). Cin8 and Kip1 were shown to be minus-end–directed as single molecules moving on single MTs under high ionic strength conditions and to switch to plus-end–directed motility under conditions of lower ionic strength and in a multi-motor MT gliding assay (*9*–*11*). Cin8 was also shown to be plus-end–directed in an antiparallel MT sliding assay under high ionic strength conditions (*10*–*12*). Deletion of the large insert in loop 8 (L8) of Cin8 enhanced its tendency to move in the minus-end direction of the MTs under low ionic strength conditions (*11*, *13*), while deletion of the C-terminal tail of Cin8 abolished the minus-end–directed preference of single-molecule motility at high ionic strength (*14*). Additional factors that have been shown to induce a switch from minus- to plus-end directionality are motor and nonmotor crowding of the MTs for Cut7 (*15*) and accumulation in clusters for Cin8 (*12*). Nonetheless, despite the above experimental and theoretical studies showing that the bidirectional motility of fungal kinesin-5s is essential for spindle assembly (*12*, *16*), the molecular mechanism of bidirectional stepping remains unclear.

A clue to unraveling this mechanism may lie in a unique feature shared by the bidirectional kinesin-5s, namely, a long N-terminal nonmotor domain (NTnmd) of ~50 to 70 amino acids whose role in regulating kinesin-5 functions remains unknown at present. This long extension is not present in exclusively plus-end–directed kinesin-5 and kinesin-1 motors (*1*, *3*), suggesting that it reflects an evolutionary adaptation of the bidirectional kinesin-5s to their functions. To reveal the function and conformation of the NTnmd, we started this study by examining intracellular phenotypes of NTnmd deletion mutants of Cin8. We found that the NTnmd is critical for the intracellular functions of Cin8 since deletions in this region produced Cin8 mutants that were not functional in cells and exhibited spindle localization defects. To investigate these defects, we conducted a cryo–electron microscopy (cryo-EM) study designed to determine the structure of the MT-bound kinesin-5 Cin8 motor containing 37 amino acids of the NTnmd. We observed a weak cryo-EM density volume close to the MTs, corresponding to the NTnmd of Cin8. Modeling and molecular dynamics simulations revealed that this region likely takes the form of an α helix that interacts with β-tubulin

[1]1Department of Chemistry, Ben-Gurion University of the Negev, Beer-Sheva 8410501, Israel. [2]Department of Molecular Biophysics and Biochemistry, Yale University, New Haven, CT 06510, USA. [3]Department of Life Sciences, Ben-Gurion University of the Negev, Beer-Sheva 8410501, Israel. [4]Ilse Katz Institute for Nanoscale Science & Technology, Ben-Gurion University of the Negev, Beer-Sheva 8410501, Israel. [5]National Institute for Biotechnology in the Negev, Ben-Gurion University of the Negev, Beer-Sheva 8410501, Israel.
*Corresponding author. Email: ranz@bgu.ac.il (R.Z.); lgheber@bgu.ac.il (L.G.)
†These authors contributed equally to this work.
‡Present address: Department of Microbiology, Institute of Medical Sciences, Banaras Hindu University, Varanasi-221 005, India.
§Present address: Department of Biomedical Engineering, Pennsylvania State University, University Park, PA, USA.

near its C-terminal tail. In in vitro experiments on MTs treated with subtilisin to remove C-terminal tubulin tails (*17*, *18*), we confirmed that the NTnmd of Cin8 interacts with the MTs via their C-terminal tubulin tails. Thus, we provide here structural and functional evidence of a noncanonical interaction between the NTnmd of a bidirectional kinesin-5 motor with MTs. In addition, we showed in a single-molecule motility assay that N-terminal deletion mutants of Cin8 exhibited a minus-end–directed bias, failing to switch from minus- to plus-end–directed motility. Last, we demonstrated that an NTnmd deletion mutant that failed to support cell viability as the sole source of Cin8 was severely defective in producing plus-end–directed antiparallel MT sliding. On the basis of our results, we propose that the noncanonical interaction of bidirectional kinesin-5s with MT C-terminal tails via the NTnmd is crucial for their bidirectional motility and intracellular functions.

RESULTS

Viability of cells expressing NTnmd deletion mutants of Cin8

The NTnmd of bidirectional kinesin-5s is considerably longer than that of the exclusively plus-end–directed kinesin-5 and kinesin-1 motors (Fig. 1A) (*3*). To examine the role of the sequences in the NTnmd in regulating the function of Cin8, we generated N-terminal deletion variants and examined their function in *S. cerevisiae* cells.

In the preparation of the N-terminal deletion mutants, the deletions were based on the division of the N-terminal extension into four segments, according to sequence similarity with other bidirectional, exclusively plus-end–directed kinesin motors, as follows (Fig. 1, A and B): (i) the most upstream N-terminal sequence between the two methionines of Cin8, i.e., M1 and M39, which is equivalent to the N-terminal extension of other bidirectional kinesin-5s but shares low sequence similarity with those motors and is rich in positively charged amino acids; (ii)

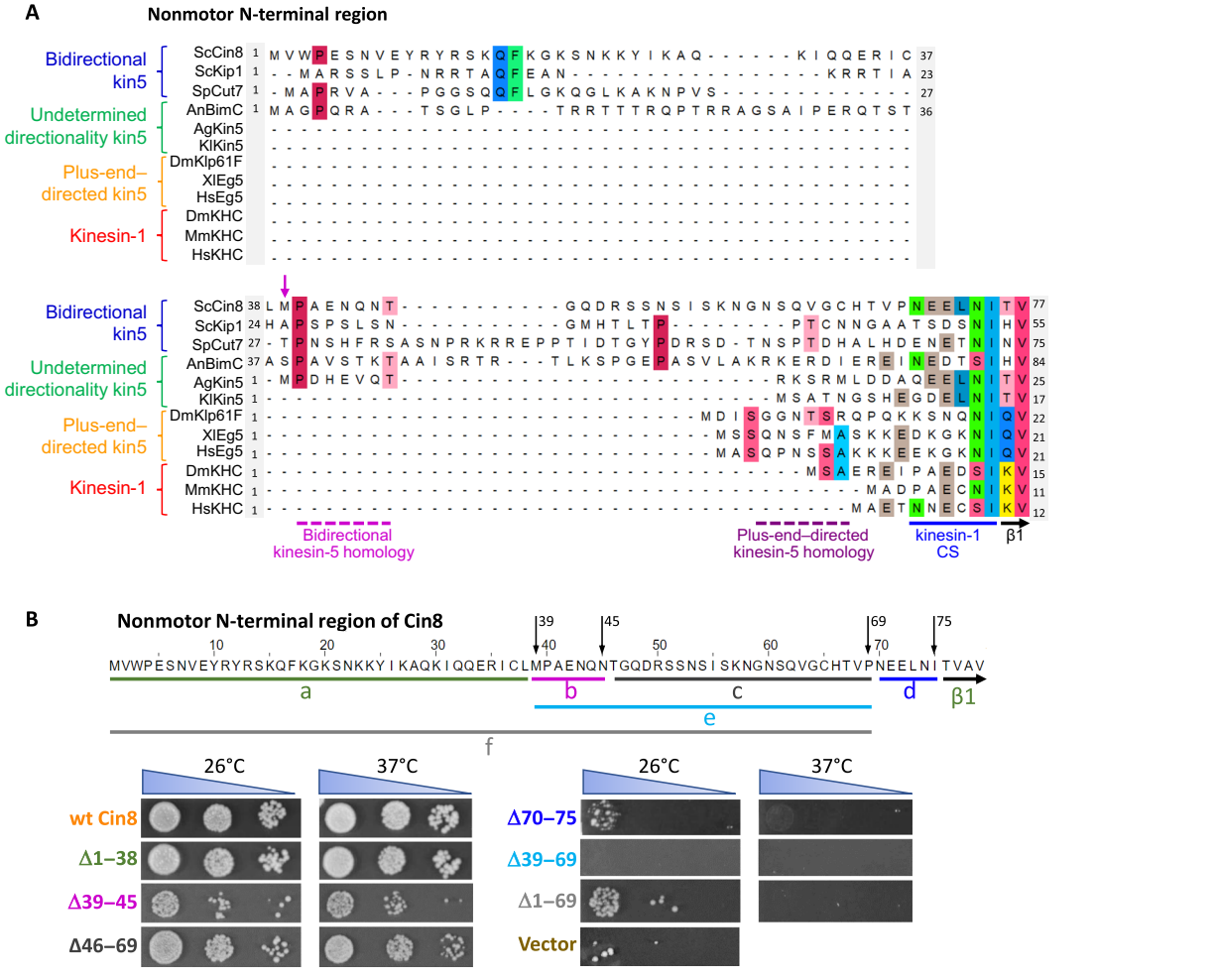

Fig. 1. Viability of cells expressing NTnmd deletion mutants of Cin8. (**A**) Multiple sequence alignment of the NTnmd of kinesin motors. Kinesin-5 (bidirectional, of undetermined directionality, and exclusively plus-end–directed) and kinesin-1 motors are indicated on the left. Structural elements are indicated on the bottom. The first and last amino acids are indicated at the beginning and the end of each sequence. The organisms are as follows: Sc, *Saccharomyces cerevisiae*; Sp, *Schizosaccharomyces pombe*; An, *Aspergillus nidulans*; Ag, *Ashbya gossypii*; Kl, *Kluyveromyces lactis*; Dm, *Drosophila melanogaster*; Xl, *Xenopus laevis*; Hs, *Homo sapiens*; Mm, *Mus musculus*. (**B**) Top: NTnmd sequence of Cin8 (amino acids 1 to 79), numbers indicate amino acid position, letters a to e indicate sequences that were deleted in the different mutants (see text). Bottom: Viability of *cin8*Δ*kip1*Δ *S. cerevisiae* cells expressing wt Cin8 or variants of Cin8 carrying deletions in the NTnmd as the sole source of kinesin-5 function. Cin8 variants are indicated on the left of each panel. Cells were plated in serial dilutions (indicated by blue triangles) at the temperatures indicated on top. "Vector," cells containing a plasmid that does not contain Cin8.

M39-N45, which shares weak similarity with parts of the N-terminal regions of bidirectional kinesin-5s and fungal kinesin-5s whose directionality is undetermined (Fig. 1A); (iii) T46-P69, which is a segment equivalent to N-terminal extensions in bidirectional and plus-end–directed kinesin-5s but exhibits low sequence homology with these kinesin-5s; and (iv) N70-I75, which is the nearest sequence to the motor domain and shares similarity with sequences believed to form the cover neck bundle (CNB) and to stabilize neck linker (NL) docking in kinesin-1 and kinesin-5s (*19*–*24*). On the basis of this division, we generated Cin8 variants that carry separate deletions of these segments (designated Cin8Δ1–38, Cin8Δ39–45, Cin8Δ46–69 and Cin8Δ70–75, respectively) or deletions of amino acids (v) M39-P69 (Cin8Δ39–69) and (vi) M1-P69 (Cin8Δ1–69).

We started by examining the ability of the N-terminal deletion variants to support cell viability as the sole source of kinesin-5 function in *S. cerevisiae* cells deleted of the chromosomal copies of *CIN8* and *KIP1* (Fig. 1B) (*25*–*27*). We had previously demonstrated that transcription of Cin8 starts from the first methionine, M1, in the NTnmd and not from M39 (*28*), and here, we showed that deletion of the first 38 amino acids of the N-terminal extension produced a variant that is functional in cells, similar to wild-type (wt) Cin8 (Fig. 1C). The variant Cin8Δ46–69 also had little impact on the viability of cells in the absence of the overlapping Kip1. The internal deletion of amino acid M39-N45 (Cin8Δ39–45) reduced cell viability at both examined temperatures, while internal deletion of the sequence nearest to the motor domain, N70-I75 (Cin8Δ70–75), almost completely abolished the viability of the yeast cells (Fig. 1B). Similar abrogation of cell viability was also caused by deletion of the first 69 amino acids of Cin8 (Cin8Δ1–69). Last, although separate deletions of amino acids M39-N45 and T46-P69 did not cause a lethal phenotype, an internal deletion that combines these two segments (Cin8Δ39–69) failed to support cell viability (Fig. 1B). These results indicate that the NTnmd is critical for the intracellular mitotic functions of Cin8 and deletion of the major part of the NTnmd (Cin8Δ1–69) produces a Cin8 that is not functional in cells.

Intracellular localization of NTnmd deletion mutants of Cin8

To further understand the defects inflicted by mutations in NTnmd (Fig. 1B), we next examined the intracellular localization of green fluorescent protein (GFP)–tagged N-terminal deletion variants in *CIN8*-deleted cells (with *KIP1* intact) expressing the tdTomato-tagged spindle-pole body component Spc42 (Fig. 2, A and B) (*9*). We divided all budded cells into four spindle morphology categories: monopolar spindles, before spindle formation, in which the two spindle pole bodies have not been separated; short bipolar spindles, less than 1.8 μm, which indicate either S-phase or metaphase cells; early anaphase spindles of 1.8 to 4 μm; and late anaphase spindles, longer than 4 μm. We found that in cells expressing Cin8Δ39–69 (i.e., the deletion that causes a lethal phenotype in *cin8*Δ*kip1*Δ cells) close to 30% of cells with monopolar spindles did not produce a Cin8-GFP signal. In contrast, in cells expressing wt Cin8, only ~7% of cells did not produce a Cin8-GFP signal (Fig. 2B). For the cells for which there was no detectable GFP signal ("no Cin8" phenotype; Fig. 2B), we concluded that Cin8 is degraded and that it is not cytoplasmatic. This finding suggests that the deletion of amino acids 39 to 69 generated a Cin8 variant that is less stable in cells, and this reduced stability may partially explain the reduced viability in cells expressing this variant as a sole source of kinesin-5. In contrast, Cin8 variants deleted amino acids 39 to 69 and 70 to 75 (Cin8Δ39–69 and Cin8Δ70–75) [which also exhibited reduced viability in *cin8*Δ*kip1*Δ cells (Fig. 1B)] exhibited a mislocalization pattern in the nucleus and/or nuclear MTs, compared to wt Cin8, which concentrated mainly at the poles (Fig. 2B and fig. S1). These findings indicate that these variants were either defective in minus-end–directed motility and/or exhibited reduced affinity to MTs (*12*, *29*). Consistently, cells expressing these two variants (Cin8Δ39–69 and Cin8Δ70–75) exhibited a considerably lower percentage of short bipolar spindles compared to wt Cin8, indicating that these variants were defective in bipolar spindle assembly (Fig. 2B). Last, cells expressing the Cin8Δ1–69 variant (which was unable to support viability in *cin8*Δ*kip1*Δ cells) also exhibited an increased percentage of mislocalized motors compared to cells expressing wt Cin8, but this difference did not reach statistical significance (Fig. 2B). Together, our results indicate that sequences within the NTnmd of Cin8 regulate the intracellular localization of this motor, mainly before spindle assembly, which, in turn, affects Cin8 functionality in cells.

Cryo-EM density map of the MT-bound Cin8 motor domain

To understand the reason behind the defective functionality and localization of NTnmd mutants, we next examined the structure of the N-terminal region by performing single-particle cryo-EM analysis of the Cin8 motor domain bound to MTs in the presence of a nonhydrolyzable adenosine 5′-triphosphate (ATP) analog, adenylyl imidodiphosphate (AMPPNP), followed by fitting a model into the cryo-EM map. Since we found that deletion of the first 38 amino acids does not interfere with Cin8 function (Fig. 1B), the Cin8 motor domain construct used for cryo-EM reconstruction started from the second methionine (M39) and contained 37 amino acids of the NTnmd (Fig. 3, A and B, and fig. S2, A to D). Previously, it had been suggested that the large 99–amino acid insert in L8 of Cin8 induces noncanonical super-stoichiometric binding of Cin8 to MTs (but was too flexible to be resolved in a cryo-EM study) (*30*). Therefore, to eliminate the effects of noncanonical MT-binding and Cin8 clustering, the large L8 of Cin8 was replaced by the equivalent 7 amino acids of the Kip1 L8 (*31*); hereafter referred to as $Cin8_{L8Kip1}$ (fig. S2, A to D). A model of $Cin8_{L8Kip1}$ was then built into the 6.1-Å resolution cryo-EM density map (fig. S2, E and F, and table S1). The local resolution map generated by the CryoRes software (*32*) indicates that the highest resolution of the obtained map is in the motor-MT interface and the less certain parts of the model are in the periphery of the map (fig. S3A). We found that the three-dimensional (3D) structure of the $Cin8_{L8Kip1}$ motor domain shares high similarity with the 3D structures of kinesin motors from other subfamilies (*33*–*35*), namely, a central β sheet with three α helices on the side facing the MTs and three α helices on the opposite side (Fig. 3, A, B, and D, and fig. S3, B and C).

Since the model of the Cin8 motor domain has not been reported before, we compared different elements of the obtained structure to those of the exclusively plus-end–directed *Homo sapiens* kinesin-5 Eg5 (crystal structure) (*36*) and of the bidirectional *S. pombe* kinesin-5 Cut7 (cryo-EM structure) (Fig. 3D and figs. S3, B and C, and S4) (*37*). The structure of the ATP-binding pocket of the $Cin8_{L8Kip1}$ motor domain is consistent with the AMPPNP-bound state (Fig. 3 and fig. S4) (*38*–*40*). The nucleotide binding and hydrolysis elements [P-loop, L9 (switch I), and L11 (switch II) (*38*–*40*)] in the 3D model of the $Cin8_{L8Kip1}$ motor domain are similar to those in Eg5 and Cut7 (Fig. 3D and figs. S3, B and C, and S4). This result is consistent with the high sequence similarity between nucleotide binding and hydrolysis elements of Cin8, Eg5, and Cut7 (fig. S4*C*).

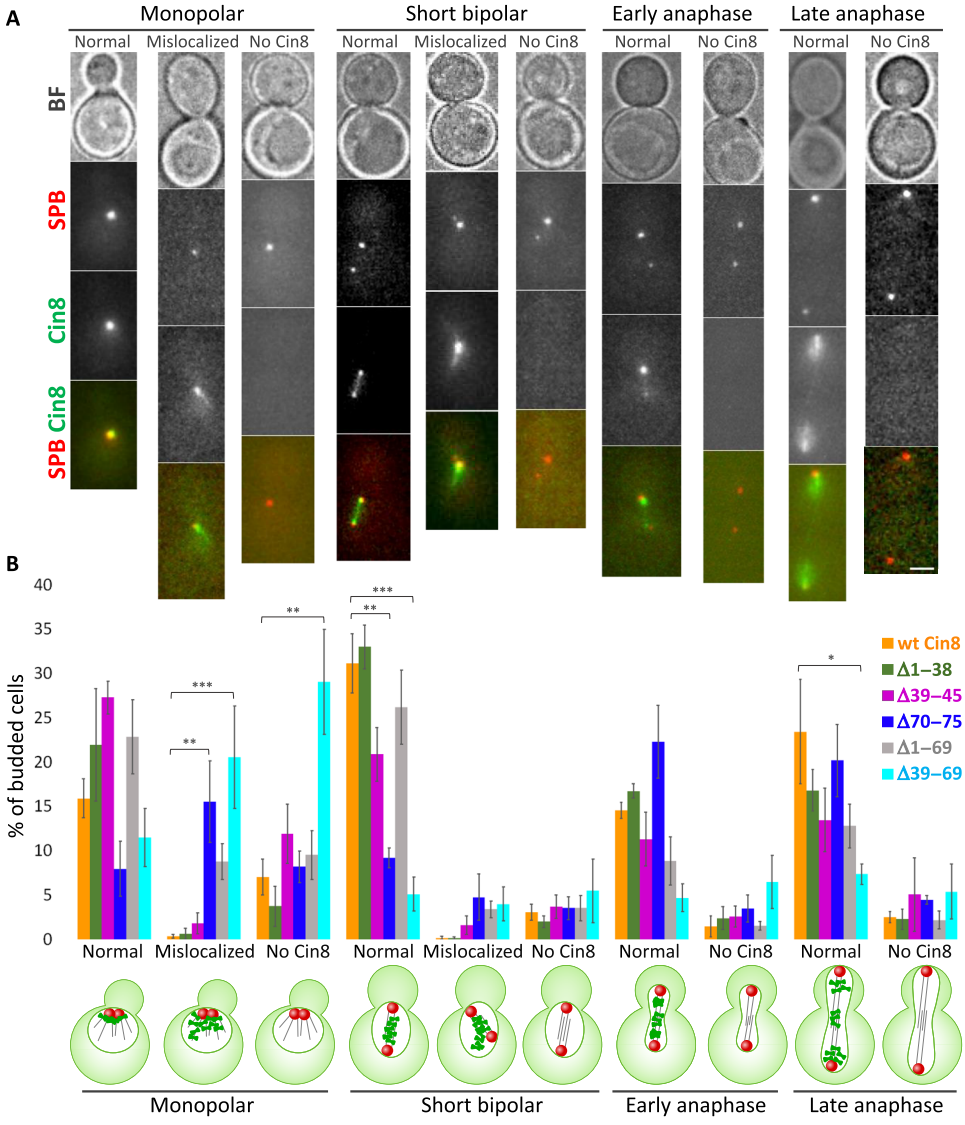

Fig. 2. Intracellular localization of GFP-tagged NTnmd deletion mutants of Cin8. *S. cerevisiae* cells used for this analysis were deleted for the chromosomal copy of *CIN8* and expressed the tdTomato-tagged spindle pole component Spc42. Cells were imaged in bright field (BF), as well as red (spindle pole body; SPB) and green (Cin8-GFP) channels. (**A**) Representative images of different spindle localization phenotypes of Cin8 variants. Scale bar, 2 μm. (**B**) Average percentage of budded cells, with different phenotypes in each spindle-length category, indicated at the bottom of the panel. Cin8 N-terminal variants are indicated on the right. A schematic representation of each localization phenotype is shown at the bottom of the panel. *$P < 0.05$, **$P < 0.01$, and ***$P < 0.001$, calculated by analysis of variance (ANOVA), followed by the Dunnett's test (*84*).

L5 of the kinesin motor domain interrupts the sequence of α2 and is located near the ATP-binding P-loop (*35, 41*). Some previous studies have shown that L5 of Eg5 regulates adenosine triphosphatase (ATPase) activity (*42–44*), and others have suggested that this loop is involved in a mechanism that gates the ATPase cycle (*45–47*). L5 has thus been investigated as a target for small-molecule allosteric inhibitors, such as monastrol and (+)-S-trityl-L-cysteine (STLC), which disrupt the ATPase cycle, thereby arresting cells in mitosis (and as a result are considered as potential anticancer agents) (*44, 48–51*). The L5 of Eg5 is three amino acids longer than the L5s of Cin8 and Cut7 (Fig. 3C), which may explain a previous report that the L5-binding inhibitor STLC does not inhibit Cut7 (*37*). According to our structure, similar to Cut7, the conformation of L5 in the presence of AMPPNP is shifted toward the plus-end of the MT compared to Eg5 (Fig. 3D). Thus, we conclude that the Cin8 L5 assumes a conformation that is different from that of the Eg5 L5 but similar to that of the Cut7 L5. In keeping with this conclusion, we found, in a single-molecule motility assay, that in the presence of 150 mM KCl and 1 mM ATP, the movement of Cin8 in the minus-end direction of the MTs is not inhibited by STLC (Fig. 3E). This finding indicates that, similar to the bidirectional Cut7, Cin8 is not inhibited by an L5-binding allosteric inhibitor.

Conformation of the NTnmd

To date, the structure of the NTnmd of bidirectional kinesin motors has not been examined, most probably because the variants used in structural studies lacked this region (*37*). The NTnmd was also absent

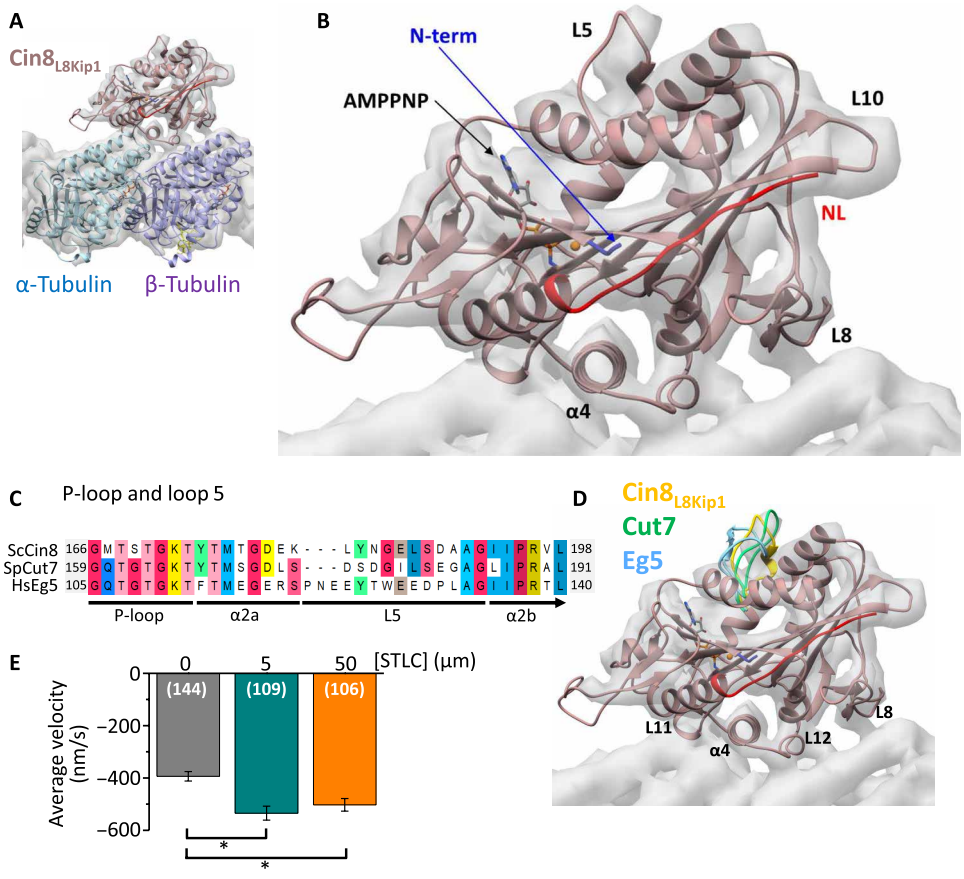

Fig. 3. Reconstruction of the MT-bound motor domain structure of Cin8$_{L8Kip1}$. (**A**) Structure of MT-bound Cin8$_{L8Kip1}$, reconstructed from the cryo-EM density map (gray) obtained in this study (EMD-10625). The reconstruction shows the Cin8$_{L8Kip1}$ motor domain (with the 99–amino acid insert in L8 replaced by seven amino acids of the L8 of Kip1), in the presence of AMPPNP attached to a Taxol-stabilized MT. (**B**) Zoom-in view of the Cin8$_{L8Kip1}$ motor domain. The color-coding is as follows: MT-bound Cin8$_{L8Kip1}$ cryo-EM density map, light gray; Cin8$_{L8Kip1}$, dusky pink; N-terminal region, blue; NL, red; α-tubulin, light blue; β-tubulin, light purple. The nucleotides are as follows: AMPPNP bound to Cin8$_{L8Kip1}$, GTP bound to α-tubulin, and GDP bound to β-tubulin. (**C**) Multiple sequence alignment of the structural elements surrounding L5, namely, P-loop, α2a, L5, and α2b. Structural elements are indicated at the bottom of the panel. (**D**) Side view of Cin8$_{L8Kip1}$ [the structural model is reconstructed from the cryo-EM density map obtained in this study, colored as in panel (B)], with Cin8$_{L8Kip1}$ L5 indicated in yellow, compared with L5 of Cut7 [Protein Data Bank (PDB): 6S8M, green] and L5 of Eg5 (PDB: 3HQD, light blue). (**E**) Effect of (+)-S-trityl-L-cysteine (STLC) on single-molecule, minus-end–directed motility of Cin8. The bar graph shows the average velocity (±SEM) calculated from a single-molecule motility assay in the absence or presence of 5 or 50 μM STLC. All the experiments were conducted at a constant concentration of 2% Me_2SO. The numbers of Cin8 motors analyzed are shown in parentheses. *$P < 0.05$; significance was calculated by ANOVA, followed by Tukey's test (*85*).

in the Cin8 variant whose density map was recently published by Bell *et al.* (*30*). We observed that the most pronounced difference between the cryo-EM density map of the Cin8 variant obtained in the present study versus the maps of the Cin8 variant reported by Bell *et al.* (*30*) and the maps of Cut7 (*37*) and of Eg5 (*47*) lies in a volume of weak density (with Gaussian filter applied) that is absent from the maps in the latter three studies (Fig. 4, A and B). This volume of weak density emerges near the MT protofilament on the same side of the motor domain where the N-terminal and the NL are located (Fig. 4). Since the variant used in the present study lacks the native large insert in the L8 of Cin8, this volume of weak density cannot be attributed to this loop. Since the Cin8 variant used here contains 37 amino acids of the NTnmd, it is very likely that the additional density results from a sequence at the N terminus of Cin8. Thus, we provide direct evidence for the conformation of the NTnmd and its possible interactions. On the basis of our analysis, the NTnmd of Cin8 probably interacts with the MT lattice between two adjacent protofilaments.

To obtain a more detailed insight into the possible structure and interactions of the NTnmd, we performed homology modeling of this region, followed by fitting to the obtained cryo-EM density map (Fig. 5). The NTnmd of Cin8 was modeled using the structure of human kinesin-13 Kif2A bound to bent αβ-tubulin heterodimers [Protein Data Bank (PDB) code: 6BBN (*52*)]. The 3D model was then fitted to the cryo-EM density, enabling refinement of the model. On the basis of this procedure, we were able to fit an additional 30 amino acids from the N terminus (N43 to E72) into the model (Fig. 5A). Following the modeling, restraint-free molecular dynamics simulations in water were used to study the structural stability and dynamics of the Cin8 3D model. The outcome of these simulations indicated that the N terminus is highly flexible, which explains why the density map for this region is weakly resolved. Although the NTnmd is highly flexible, the simulation outcome indicates that this region highly populates a conformation in which it interacts with tubulin (fig. S5).

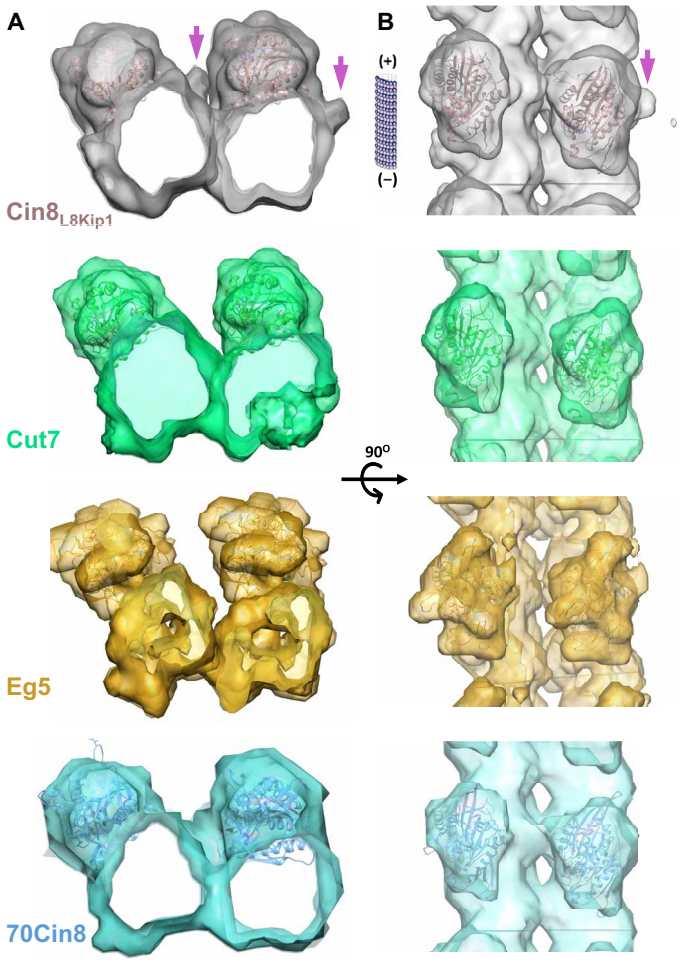

Fig. 4. Cryo-EM density map of the NTnmd of $Cin8_{L8Kip1}$. Cryo-EM density map of $Cin8_{L8Kip1}$ bound to MTs obtained in this work (light gray), compared to the density maps of Cut7 (EMD-3527, PDB: 6S8M, green) (*37*), Eg5 (EMD-2077, PDB: 4AQV, yellow) (*47*), and a Cin8 variant lacking the first 70 amino acids of the N-terminal region (EMD-8408, with a model of Cin8 obtained in this study, 70Cin8, blue) (*30*), all bound to MTs. (**A**) Cross-sectional view (from minus- to plus-end of the MTs). (**B**) A perpendicular-to-MT view; directionality of the MT is indicated on the left, at a 90° rotation compared to (A). The 70Cin8 variant includes the 99–amino acid insert in L8 of Cin8. Its density map was obtained in the presence of ADP-AlF_x which corresponds to the ADP-Pi nucleotide state. All density maps (except for the density map of Eg5, which has a 9.7-Å resolution) were filtered to a lower resolution of 20 Å to prevent artifacts. The most pronounced difference between the four structures is a low-intensity feature in the $Cin8_{L8Kip1}$ cryo-EM density map (mauve arrows), which is absent from the cryo-EM density maps of Cut7, Eg5, and 70Cin8. This feature is proximal to the N terminus of the motor domain, making contact with the tubulin surface and extending toward the $Cin8_{L8Kip1}$ motor domain bound to the adjacent MT protofilament. Models were fitted to the maps using the "fit in map" feature of UCSF-Chimera (*75*).

The cryo-EM fitted model reveals that to fit this weak cryo-EM density map (Fig. 4), the NTnmd must undergo a turn that diverts it away from the NL (Fig. 5, green arrow). The model of the N-terminal region also displays an α helix (amino acids Q48 to N60), whose distal N-terminal end lies in proximity to β-tubulin (Fig. 5), close to its C-terminal tail (fig. S6). Nonetheless, the resolution of this extra weak density was not sufficient to unambiguously define the conformation or the exact placement of this predicted helix.

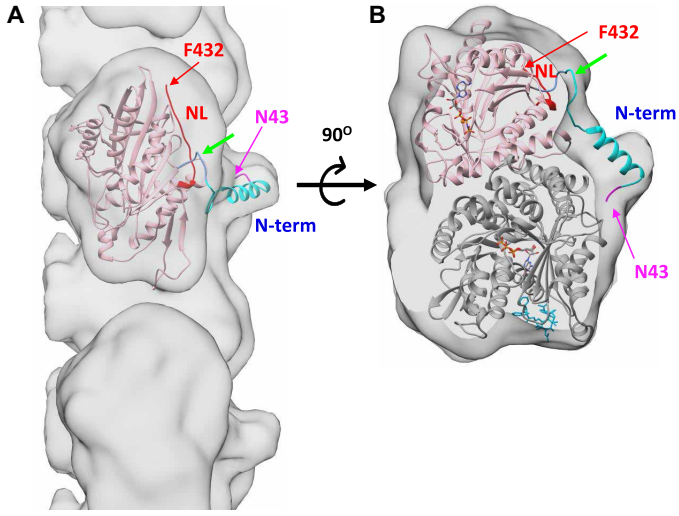

Fig. 5. Modeling analysis reveals a unique orientation of the NTnmd and its possible interaction with β-tubulin. (**A** and **B**) Top (A) and back (B) views of the molecular model based on the cryo-EM structure and the weak intensity volume obtained in this work. Color-coding is as follows: $Cin8_{L8Kip1}$, pink; NL, red; N70-I75, blue; T46-P69, cyan; N43-N45, magenta. The first and last Cin8 amino acids of this model, N43 and F432, are indicated. Green arrows indicate the approximate position of the turn that causes the NTnmd to deviate away from the NL.

In vitro motor activity of NTnmd Cin8 variants on subtilisin-treated MTs

The structural data presented here suggest that, upon MT binding, Cin8 interacts with the C-terminal tails of tubulin via its NTnmd (Figs. 4 and 5 and fig. S6). To directly test this mechanism of interaction, we examined the binding and motility of wt and selected NTnmd mutants of Cin8 on MT treated with subtilisin, an agent that has been shown to remove C-terminal tubulin tails (Figs. 6 and 7) (*17*, *18*). To this end, we used a single-molecule motility assay, in which we characterized the activity of GFP-tagged full-length N-terminal variants, overexpressed and purified from *S. cerevisiae* cells, on fluorescently labeled GMPCPP-stabilized polarity-marked MTs (*12*, *53*). These experiments were conducted in the presence of 1 mM ATP and 70 mM KCl. At higher salt concentrations, no binding of wt Cin8 to subtilisin-treated MTs was observed, indicating that C-terminal tubulin tails facilitated Cin8 binding to MTs in high-salt solutions. We observed MT binding and processive unidirectional motility of wt Cin8 and its NTnmd deletion mutants (Fig. 6). Following treatment of plus-end–labeled MTs with subtilisin, very few MTs retained their plus-end labeling. Nonetheless, we were able to confirm processive minus-end–directed motility for wt Cin8 and NTnmd mutants on those MTs that retained their plus-end labeling (Fig. 6A). To determine the velocity of Cin8 variants on subtilisin-treated MTs, we performed mean square displacement (MSD) analysis of motility trajectories (Fig. 6B) (*9*, *11*, *54*). MSD analysis was chosen because it does not require polarity labeling of the MTs and produces similar results to mean displacement (MD) analysis (*11*). We found that for wt Cin8, velocity on subtilisin-treated MTs was considerably higher than on untreated MTs (Fig. 6B). This result further supports the notion that C-terminal tubulin tails contribute to MT binding of Cin8. In addition, on untreated MTs, the velocity of the NTnmd deletion mutants was faster than that of the wt Cin8 (Fig. 6B). As discussed below (Fig. 8 and Table 1), this result indicates a weaker interaction

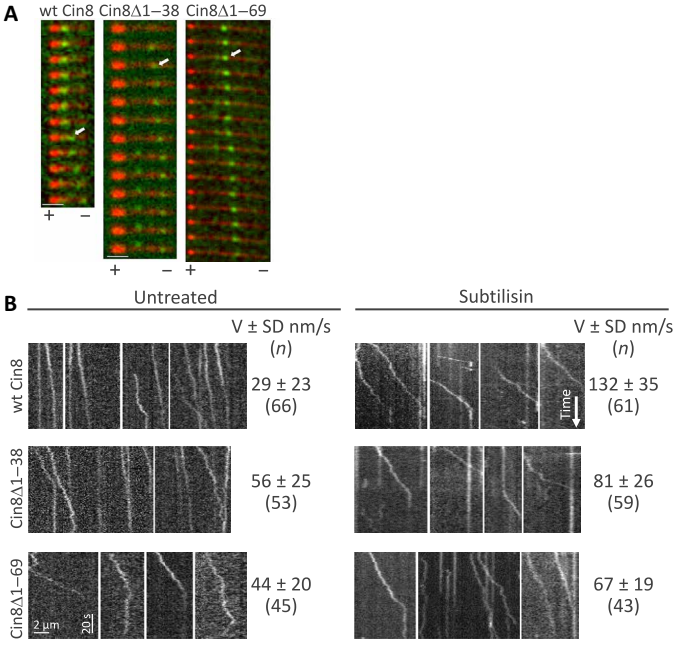

Fig. 6. Motility of wt Cin8 and NTnmd deletion mutants on subtilisin-treated MTs. (**A**) Time-lapse recordings of Cin8-GFP motor motility (green) on polarity-marked, subtilisin-treated MTs (red). Bright red seeds indicate the plus-end labeling of the MTs. Cin8 variants are indicated on the top of the panel. Arrows point to the Cin8-GFP motors moving processively in the minus-end direction, away from the plus-end red bright seed. The polarity of the MTs is indicated at the bottom of the panel. Scale bar, 2 μm; time intervals: 10 s. (**B**) Representative kymographs and average velocities (*V*) ± SD of wt Cin8 and NTnmd deletion mutants Cin8Δ1–38 and Cin8Δ1–69, indicated on the left, in the presence of 70 mM KCl and 100 μM ATP. MTs were either untreated (left) or treated with subtilisin (right), indicated on the top of the panel. Since not all the MTs retained their polarity mark, average velocity (*V*) was determined using mean square displacement analysis (*9*, *11*). Velocities are indicated on the right of each kymograph set. Numbers in parentheses indicate the number of moving motors in each case.

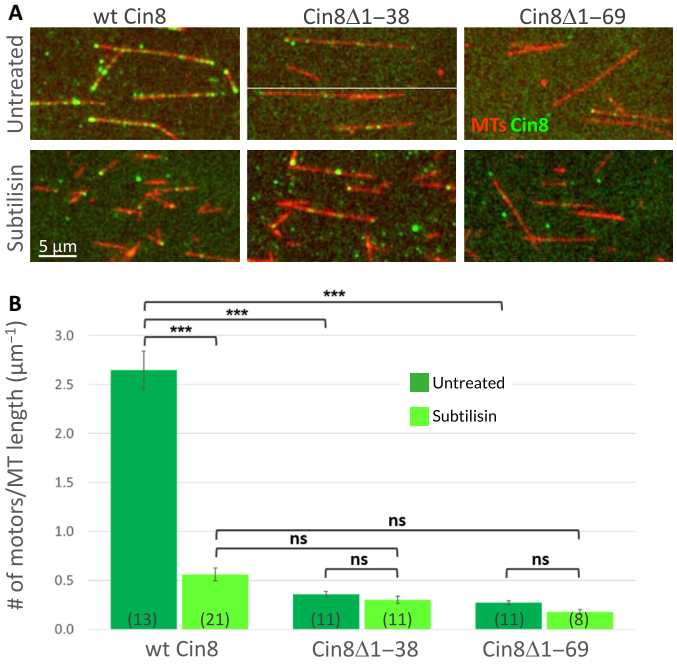

Fig. 7. Binding of Cin8 NTnmd variants to subtilisin-treated MTs. (**A**) Representative images of Cin8 (green) bound to surface-attached MTs (red), in the presence of 100 μM ATP. Cin8 variants are indicated at the top of the figure. MTs were either untreated (top) or treated with subtilisin (bottom), as indicated on the left. (**B**) Average number of motors per micrometer of MT length (±SEM) for Cin8 bound to surface-attached MTs in the presence of ATP, in 500-μm^2 fields. Numbers of analyzed fields are indicated in parentheses. ***$P < 0.001$; ns, not significant. Significance was evaluated using ANOVA, followed by Tukey's test.

with MTs of the NTnmd mutants compared to the wt Cin8. In contrast, on subtilisin-treated MTs, velocities of the NTnmd mutants were considerably lower, compared to the wt Cin8 (Fig. 6B, right), indicating that the effect of the NTnmd on the motility of Cin8 is strictly dependent on the presence of C-terminal tubulin tails.

We next examined the binding of wt Cin8 and NTnmd deletion to the MTs by determining the number of Cin8 motors bound to subtilisin-treated MTs compared to untreated MTs in the presence of ATP (Fig. 7) (*13*, *29*). First, we found that on untreated MTs, the number of NTnmd mutants (Cin8Δ1–38 and Cin8Δ1–69) bound to MTs was markedly reduced compared to the wt Cin8 (Fig. 7). This result indicates that the NTnmd of Cin8 is directly involved in the MT binding of Cin8. We found that treatment with subtilisin reduced the number of wt Cin8 motors bound to MTs (Fig. 7). This result indicates that the C-terminal tubulin tails are directly involved in Cin8 binding to the MTs since, in their absence, Cin8 binding to MTs is reduced. Treatment with subtilisin did not affect the binding of the NTnmd deletion mutants to the MTs (Fig. 7), indicating that when NTnmd is deleted, partially or completely, the C-terminal tubulin tails do not contribute to MT binding of Cin8. Thus, this result strongly supports the notion that the NTnmd induces MT binding via direct interaction with the C-terminal tails.

Directionality switch and antiparallel MT sliding of NTnmd-deleted mutants of Cin8

To further understand the relationship between the motor functions of NTnmd mutants of Cin8 and their intracellular defects (Figs. 1B and 2), we examined the motile properties of the variants in vitro. Experiments were performed at a saturating ATP concentration and at an intermediate ionic strength (110 mM KCl) since, under high ionic strength conditions, some N-terminal deletion mutants failed to bind to MTs. We have previously demonstrated that one of the factors that affect the directionality and velocity of Cin8 is its accumulation in clusters on MTs (*12*, *54*) and that MT-bound motile clusters of Cin8 can split and merge while remaining motile, indicating that these clusters are active motors and not merely nonfunctional aggregates (*54*). Thus, here, we examined the effects of mutations in the N-terminal region on the motility of single molecules and clusters separately. For this purpose, we sorted single molecules from clusters of Cin8, based on their fluorescence intensities, as previously described (*54*); see also Materials and Methods. We found that under the examined conditions, consistent with previous reports (*11*, *55*), single molecules and clusters of wt Cin8 moved in a bidirectional manner, exhibiting motility trajectories in both plus- and minus-end directions on the MTs (Fig. 8).

The motile behavior of the Cin8Δ70–75 variant with the internal deletion of amino acids 70 to 75 [a sequence homologous to the N-terminal region of kinesin motors that is believed to form the CNB and stabilize NL docking (*19*–*24*)] differed markedly from the behaviors of the wt Cin8 and variants with other N-terminal deletions (Fig. 8 and

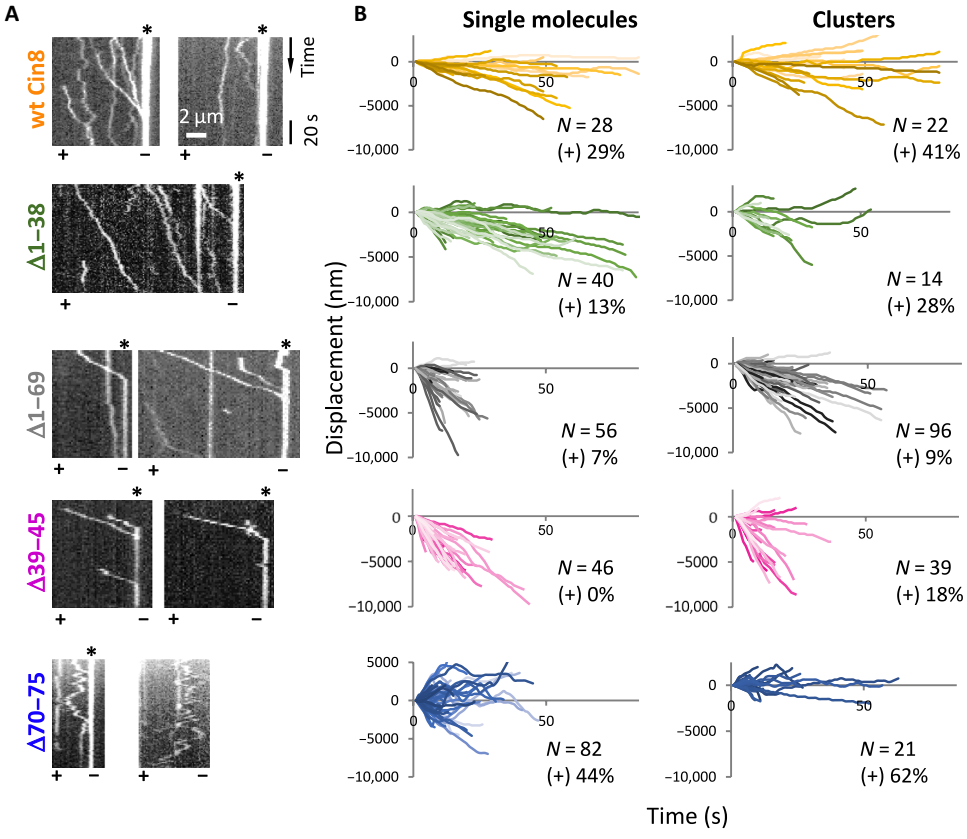

Fig. 8. In vitro single-molecule motility of N-terminal deletion Cin8 variants. (**A**) Representative kymographs of movements of Cin8 N-terminal variants in the presence of 110 mM KCl. The polarity of the MTs is indicated at the bottom of each kymograph. Asterisks indicate Cin8 clustering at minus-ends of the MTs. (**B**) Trajectories of motility of Cin8 N-terminal deletion variants. The trajectories of single molecules (left) and clusters (right) were used for the analysis of motile properties. Differentiation between single motors and clusters was performed as previously described (*13, 54*). The number of trajectories and the percentage of movements toward the plus-ends of MTs are indicated at the bottom right of each graph. Cin8 variants for (A) and (B) are indicated on the left of the figure.

fig. S7). While the other Cin8 variants exhibited processive motility in either the minus- or plus-end directions, the Cin8Δ70–75 mutant exhibited bidirectional motility with frequent changes in directionality within the same run (Fig. 8 and fig. S7). To determine whether this behavior was ATP-dependent, we examined the motility of Cin8Δ70–75 in the presence of adenosine 5′-diphosphate (ADP) (fig. S7). In contrast to wt Cin8, which exhibited a minus-end–directed bias in the presence of ATP but not ADP, the displacement of Cin8Δ70–75 was symmetrically bidirectional, with similar instantaneous displacement distributions in the presence of either one of the nucleotides. These results indicate that the motility of Cin8Δ70–75 was ATP-independent and was mainly diffusion-driven (fig. S7). In keeping with these findings, it was previously demonstrated that, in the absence of N-terminal sequences, the NL of the human kinesin-5 Eg5 was unable to dock onto the motor domain (*56*). Thus, our results indicate that, similar to kinesin-5 Eg5, at least part of the amino acids 70 to 75 sequence of Cin8 may serve as a cover strand, enabling CNB formation during the ATPase cycle, which is essential for NL docking, correct ATPase activity, and ATP-dependent motility.

Examination of the motility of other N-terminal variants revealed that deletion of the first 38 amino acids (Cin8Δ1–38) decreased the percentage of Cin8 clusters bound to MTs (Fig. 8B and Table 1), which indicates that the first 38 amino acids of Cin8 contribute to the accumulation in clusters of MT-bound Cin8. In contrast, deletion of the first 69 amino acids of the N terminus of Cin8 increased the percentage of clusters of MT-bound motile Cin8 (Fig. 8 and Table 1). The average intensities of the wt and Cin8Δ1–69 clusters [in arbitrary units (a.u.)] were not statistically different [254 ± 8 (SEM; $n = 22$) versus 310 ± 22 (SEM; $n = 87$) for wt and Cin8Δ1–69, respectively]. Although the mechanism by which the deletion of NTnmd increases motor clustering is not clear, a possible explanation for this finding is that motor clustering contributes to the stability of this mutant (Cin8Δ1–69).

We found—for both single molecules and clusters of Cin8 variants—that all the deletions in the N-terminal region, except for amino acids 70 to 75, increased the minus-end–directed bias of Cin8 motors, thereby increasing the percentage of trajectories in the minus-end direction and also increasing their velocity (Fig. 8 and Table 1). We have previously demonstrated that decreasing the affinity between Cin8 and MTs, either by increasing the ionic strength or by introducing a negatively charged phospho-mimetic mutation at the motor-MT interface, increased the minus-end–directed bias, thereby increasing the percentage and velocity of minus-end–directed trajectories (*11, 55*). Together, those results and the findings of the current study suggest that deletions in the N-terminal region decrease the affinity of Cin8 for the MTs, supporting the notion that the sequences of the N-terminal region of Cin8 contribute to direct motor–MT interactions. We also found that the deletion of these sequences of the N-terminal region decreased the

Table 1. Motile properties of the N-terminal deletion Cin8 variants. MD analysis was used for the determination of velocities (*V*), durations of motile episodes, percent of total runs longer than 60 s, and percentages of plus-end–directed movements for Cin8 N-terminal variants that exhibit directional motility. Negative values of velocity represent motility in the minus-end direction of the MTs; *n*, number of Cin8 motors analyzed.

	Monomers					Clusters					
Cin8 variant	***V* ± SD (nm/s)**	**Duration of motile episodes ± SEM (s)**	**% of (+)-end movements**	**% of total runs >60 s**	***n***	***V* ± SD (nm/s)**	**Duration of motile episodes ± SEM (s)**	**% of (+)-end movements**	**% of total runs >60 s**	***n***	**% of clusters**
wt Cin8	−32 ± 0.4	38 ± 4	29	17	28	−18 ± 1	44 ± 5	41	23	22	44
Δ1–38	−65 ± 1	34 ± 4	13	23	40	−56 ± 1	29 ± 4	28	29	14	26
Δ1–69	−175 ± 2	11 ± 1	7	2	56	−107 ± 1	18 ± 1	9	24	96	63
Δ39–45	−281 ± 5	13 ± 1	0	0	46	−205 ± 1	12 ± 1	18	13	39	48

duration of motile episodes and the total duration of motile runs of both single molecules and clusters of Cin8 (Fig. 8 and Table 1). This result is also consistent with the decreased affinity between the mutant motors and MTs. Last, we recently proposed a molecular model that explains the directionality switch from minus- to plus-end–directed motility. According to this model, any force that opposes the minus-end–directed motility of Cin8 (referred to as drag) induces a change to the plus-end direction (*54*). Thus, the NTnmd, which induces such a switch (Fig. 8 and Table 1), exerts a drag force on the moving Cin8, consistent with increased MT binding by Cin8 via its NTnmd.

Deletion of the first 38 amino acids caused the smallest effect on the motility of Cin8, as is consistent with the finding that this variant does not affect cell viability when expressed as the sole source of kinesin-5 function (Fig. 1B); this finding thus demonstrates a correlation between effects on motor motility and cell viability. Consistently, deletions of the first 69 amino acids and amino acids 39 to 45 produced the most pronounced effect on motor motility (Fig. 8 and Table 1) and markedly affected cell viability (Fig. 1B).

As mentioned above, we have previously demonstrated that accumulation in clusters of MT-bound motors is one of the major factors that induces a directionality switch from fast minus-end–directed motility to slow plus-end–directed motility of Cin8 (*12, 54*). In the current study, deletions within the NTnmd markedly reduced the percentage of plus-end–directed trajectories of single molecules and clusters, compared to wt Cin8 (Fig. 8B and Table 1). The deletion of almost the entire NTnmd (Cin8Δ1–69) produced the most dramatic effect: In this variant, 63% of the moving motors clustered, but only 9% of those clusters moved in the plus-end direction of the MTs (Fig. 8B and Table 1). In comparison, 43% of the moving wt Cin8 motors clustered, and 41% of those clusters moved in the plus-end direction of the MTs (Fig. 8B and Table 1). Thus, our results clearly indicated that deletions within the NTnmd reduce the ability of Cin8 clusters to switch directionality from minus- to plus-end–directed motility.

An additional condition under which Cin8 has been demonstrated to be plus-end–directed is during sliding apart antiparallel MTs in vitro (*10*–*12*). This plus-end–directed motility is believed to enable kinesin-5s, Cin8 included, to separate the spindle poles apart when performing their critical role in spindle assembly (*12*). Since deleting the whole NTnmd of Cin8 (Cin8Δ1–69) prevented the switch from minus- to plus-end–directed motility upon motor clustering in the single-molecule motility assay (Fig. 8 and Table 1), we examined how this mutation affects the ability of Cin8 to produce plus-end–directed antiparallel MT sliding in vitro (Fig. 9). For this purpose, we labeled the plus-ends of the MT with a bright rhodamine seed (*12*) and polymerized two sets of MTs, in the presence and absence of biotin-labeled tubulin. The biotinylated MTs were attached to the surface, followed by the addition of biotin-lacking MTs in the presence of Cin8 (*12*, *29*). Consistent with previous reports (*10*, *12*, *29*), we observed that the majority of antiparallel MT sliding events (86%) mediated by the wt Cin8 were plus-end–directed (Fig. 9 and movie S1), as is to be expected from the physiological functions of Cin8 in spindle assembly. In contrast, only a third of the MT sliding events produced by Cin8Δ1–69 were plus-end–directed. For this mutant, we found similar percentages of minus- and plus-end–directed antiparallel MT sliding events and bidirectional MT sliding (Fig. 9 and movies S2 to S4). The average velocity of plus-end–directed sliding events of the Cin8Δ1–69 mutant was significantly faster than that of the wt Cin8 (Fig. 9), similar to the result obtained in the single-molecule motility assay in the minus-end direction (Figs. 6 and 8 and Table 1). These results indicate that deletion of the NTnmd severely impairs the plus-end–directed motility of Cin8 during the sliding of MTs. Since minus-end–directed and bidirectional MT sliding cannot contribute to spindle pole body (SPB) separation during spindle assembly, this sliding behavior is likely to be the reason for the severely defective viability of *S. cerevisiae* cells expressing the Cin8Δ1–69 variant as the sole source of kinesin-5 activity (Fig. 1B). This result is also consistent with the notion that—in addition to directly increasing the MT-motor interactions—the NTnmd regulates the directionality of Cin8: The deletion of the NTnmd greatly reduces the ability of Cin8 to move in the plus-end direction of the MTs under a variety of experimental conditions.

Together, our structural and motility data indicate that sequences in the NTnmd of Cin8 interact with the MT lattice via the C-terminal tubulin tails. This interaction increases the affinity of Cin8 for MTs and affects its velocity, directionality, and ability to induce plus-end–directed antiparallel MT sliding, thus indicating the importance of the NTnmd for the intracellular functions of Cin8.

DISCUSSION

The bidirectional kinesin-5s share a large NTnmd of 50 to 70 amino acids, which is not found in the exclusively plus-end–directed

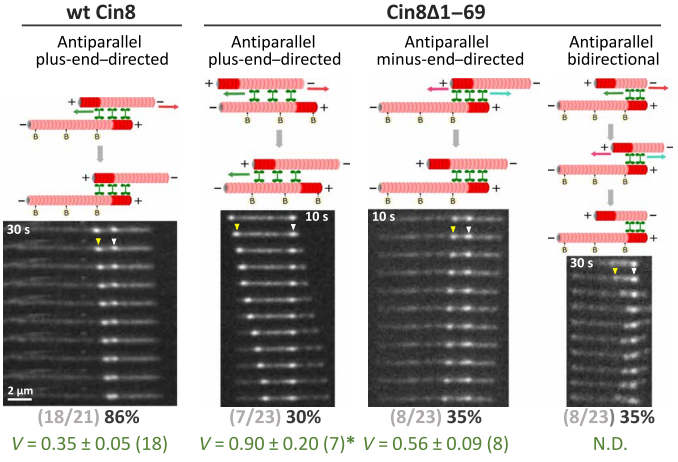

Fig. 9. Antiparallel MT sliding induced by wt Cin8 and Cin8Δ1–69. Representative time-lapse recordings of different MT sliding events are presented, as indicated at the top of the figure. For wt Cin8, plus-end–directed antiparallel MT sliding is shown (movie S1); for Cin8Δ1–69, plus-end–directed (movie S2), minus-end–directed (movie S3), and bidirectional (movie S4) antiparallel MT sliding are shown. The time interval between the frames is indicated at the top of each time-lapse sequence; total run time: 300 s. White arrowheads indicate the stationary plus-end bright label of the surface-attached MTs. Yellow arrowheads indicate the mobile plus-end bright label of the sliding MTs. Top: Schematic representations of the different sliding events. Rhodamine-labeled MTs are shown as light-red tubes; plus-end labeling is indicated by dark red coloring of the MTs; surface binding of the MTs via an avidin-biotin bond is indicated by "B"; Cin8 motors are shown as green vertical dumbbell shapes; MT polarities are indicated by "+" and "–"; red and magenta arrows indicate the direction of movement of the sliding MT; green arrows indicate plus-end directionality of the motors; and cyan arrows indicate minus-end directionality of the motors. Numbers (light gray) and percentages (dark gray) of the different categories of MT sliding for each variant are indicated at the bottom of the figure. Average velocities *V* (±SEM) for the different MT sliding categories are indicated in green at the bottom of the figure. Numbers in parentheses indicate the number of events. $*P < 0.05$, compared to plus-end–directed sliding of wt Cin8, calculated by ANOVA followed by Tukey's test.

kinesin-5s. The role of this domain in the regulation of the motile properties and intracellular functions of the bidirectional kinesin-5s has not yet been established. To determine the role of this domain in the function of the bidirectional kinesin-5 Cin8 motors, we combined intracellular and in vitro experiments with N-terminal deletion mutants and a cryo-EM study to examine the structure of the motor domain of Cin8 bound to MTs in the presence of AMPPNP.

Reconstruction of the structure of the Cin8 motor domain revealed that it exhibits the features of canonical binding to MTs, similar to kinesin-like motors, with the NL orienting in the plus-end direction of the MT in the presence of AMPPNP. However, in contrast to the previously published structures of MT-bound kinesin-5s (*4, 15, 24, 30, 37, 42, 47, 57*), the Cin8 used in this study contained an additional 37 amino acids in its N terminus, upstream of the motor domain, thus enabling us to examine the structure of this region for MT-bound Cin8. The presence of these 37 amino acids was manifested in additional cryo-EM density located close to the MT lattice (Figs. 4 and 5). Such a density element is absent from the MT-bound motor domains of other bidirectional and exclusively plus-end–directed kinesin-5s that lack the NTnmd. This finding indicates that it is likely that this N-terminal region of Cin8 interacts directly with MTs (Fig. 5). This mechanism of interaction between the NTnmd of Cin8 and the C-terminal tubulin tails was further supported by in vitro experiments on MTs treated with subtilisin (Figs. 6 and 7), which was previously demonstrated to cleave C-terminal tubulin tails (*17*, *18*). Although the interaction of the NTnmd with MTs was previously suggested for the bidirectional *S. pombe* kinesin-5 Cut7 (*15*), our work provides direct structural and functional evidence for such interaction for a bidirectional kinesin-5 motor. Moreover, we demonstrated that the deletion of sequences in this region produced phenotypic defects in intracellular functions, with the deletion of the first 69 amino acids resulting in a severely defective Cin8 mutant that was unable to support yeast cell viability as the sole source of kinesin-5 function (Fig. 1B). In addition, we demonstrated that the motile and MT binding properties of these deletion mutants were consistent with their reduced affinity to MTs (Table 1). We also showed that the N-terminal deletion mutants exhibited an impaired ability to switch directionality from minus- to plus-end–directed motility (Fig. 8), which is important for their intracellular functions (see below). Last, we demonstrated that deletion of the entire NTnmd impaired the ability of that variant to produce efficient plus-end–directed antiparallel MT sliding (Fig. 9), which was consistent with its inability to support cell viability as the sole source of kinesin-5 function (Fig. 1B). Together, these findings provide direct structural evidence that the NTnmd of a bidirectional kinesin-5 motor facilitates noncanonical MT binding, which is important for its motile properties and intracellular functions.

As mentioned above, the structural and functional data presented here suggest that the NTnmd of Cin8 interacts with the C-terminal tail of β-tubulin (Figs. 5 to 7 and fig. S6). A similar concept was recently demonstrated for the positively charged insertion in loop 12 (K-loop), which is unique to the kinesin-3 subfamily: It was demonstrated that the presence of the K-loop increases the ATPase rate and MT affinity in the kinesin-3 homolog Kif1B (*58*). Moreover, it was demonstrated that the K-loop increases the initial attachment rate of the kinesin-3 KIF1 to MTs (*59, 60*) by inducing a weak MT interaction in the presence of ADP (*60*). It was also suggested that an α helix immediately adjacent to the K-loop facilitates a specific conformation of the K-loop that is essential for its function (*61*). Last, it was demonstrated that the motility of Kif1A is regulated by pauses induced by interactions between the K-loop and the polyglutamylated tubulin C-terminal tails (*62*). Thus, it is possible that, similar to the kinesin-3 motors, the bidirectional kinesin-5s interact with the tubulin C-terminal tail, via the NTnmd, to enable their unique motor functions.

It is, however, puzzling why noncanonical binding to the MTs is required for bidirectional kinesin-5 motor function. It has previously been reported that processive plus-end motility of kinesin-1 motors is achieved, in part, by a gating mechanism that prevents simultaneous strong binding of the two kinesin-1 motor domain heads to MTs (*63*). It has also been reported that for kinesin-1 to take steps in the minus-end direction, the motor had to be mutated to enhance the flexibility of the NL, thereby enabling the production of a two-headed MT-bound state (*64*). On the basis of the findings of the current study, we propose that the noncanonical binding to MTs via the NTnmd enables the MT two-headed bound state, which may be one of the intermediate states leading to bidirectional stepping. Two of our recently published studies support this notion. In the first, we demonstrated that the large insert in L8 of Cin8 can bind MTs, without canonical MT binding on the motor domain of Cin8. We also demonstrated that the deletion of this large insert is essential for bidirectional motility on the single-molecule level and in surface MT gliding assays (*13*). In the second study, we demonstrated that the flexibility

of NL anchoring to the motor domain of Cin8 is essential for Cin8 functionality (*29*). In light of the knowledge that flexibility of the NL is correlated with the two-headed MT bound state of plus-end–directed kinesin-motors (*65*–*67*), it is possible that the flexibility of the NL docking of Cin8 may also enable the two-headed bound state, enabling stepping in two directions. Thus, we propose that the noncanonical MT binding of Cin8, via the conserved NTnmd and the large insert in L8, together with the flexible NL docking provide the necessary molecular conditions enabling bidirectional motility.

The three bidirectional kinesin-5s reported to date are motors of fungal cells (*8*–*11*). We have recently proposed a physiological role for the bidirectional motility of kinesin-5s in these cells, in which the nuclear envelope does not break down during mitosis. In contrast to higher eukaryote cells, the dynein motor does not participate in the initial spindle pole separation during mitotic spindle assembly in fungal cells (*1*, *3*). We thus proposed that the minus-end–directed motility of kinesin-5s is required to locate these motors near the spindle poles before spindle assembly. At this location, the motors cluster and capture MTs from neighboring poles. Then, by switching from minus- to plus-end–directed motility, clusters of Cin8 slide apart the captured MTs from neighboring poles (*12*), providing spindle pole separation and spindle assembly. On the basis of this model, the ability to switch from minus- to plus-end–directed motility is critical for the mitotic function of fungal kinesin-5s. One of the marked differences between the motile properties of wt Cin8 and the NTnmd mutants is the inability of the mutants to switch to plus-end–directed motility—as single molecules and as clusters (Fig. 8 and Table 1). Last, deletion of the greater part of the NTnmd severely impairs the ability of the mutant to produce plus-end–directed antiparallel MT sliding (Fig. 9), which in turn, causes defects in spindle pole separation and formation of the mitotic spindle (*12*). We thus conclude that the defective intracellular functionality of the NTnmd mutants, especially that of Cin8Δ1–69 (Figs. 1B and 2), results from their reduced affinity to MTs and their inability to switch to plus-end–directed motility and to produce plus-end–directed MT sliding (Figs. 8 and 9 and Table 1). These defective motility properties are the direct outcome of the absence of noncanonical MT binding of the NTnmd mutants.

Although members of the kinesin superfamily share homology in elements that are involved in the ATPase cycle and canonical MT binding, the different subfamilies have evolved unique structural elements that enable specific motile and mechanical properties adapted to their intracellular functions. The data presented here indicates that the NTnmd of Cin8 serves as such an element, enabling the noncanonical MT binding that is essential for its motor and intracellular functions. Since the NTnmd is a feature common to bidirectional kinesin-5s, it is likely that the NTnmd is essential for the ability to step in two directions and the intracellular functions of these motors.

MATERIALS AND METHODS

Protein expression and purification

All the functional in vivo and in vitro assays were performed on full-length Cin8 variants that carried only deletions in the NTnmd. Since the stalk (bipolar assembly domain) and tail of these variants remain intact, they are predicted to be tetramers and to localize properly to the nucleus (*5*, *28*, *57*). Only the construct used for the cryo-EM study lacked the large L8 of Cin8 (replaced by the short L8 of Kip1). This L8-deleted construct was used so as to eliminate super-stoichiometric MT binding [with ~4 motor domains bound to one tubulin dimer (*30*)] and to prevent possible masking by the large L8 (*30*) of the density contributed by the NTnmd in the cryo-EM map.

For cryo-EM analysis, the sequence encoded for the $Cin8_{L8Kip1}$ monomeric motor domain [in which the NTnmd started from M39 and in which the 99–amino acid insert in L8 of Cin8 (amino acids 255 to 353) was replaced with the corresponding 7–amino acid sequence of Kip1 (amino acids 234 to 240 of Kip1) (fig. S2, A and B)] was cloned into the $pET26B^+$ vector, with the addition of a 6× His-tag at the C terminus of the construct. Expression of the 6× His-tagged $Cin8_{L8Kip1}$ construct was induced in 250 ml of BL21-CodonPlus (DE3)-RIPL cell culture with 0.2 mM isopropyl-β-D-thiogalactopyranoside (IPTG). The culture was incubated at 18°C for 6 hours, after which the cells were harvested by centrifugation at 5000 rpm for 15 min at room temperature and resuspended in lysis buffer [50 mM Hepes, 500 mM KCl, 10 mM $MgCl_2$, Triton X-100 0.01%, 0.5 mM tris(2-carboxyethyl)phosphine (TCEP), and 10% glycerol (pH 7.5)]. Cells were disrupted with a probe-type ultrasonicator, followed by centrifugation at 13,500 rpm for 30 min at 4°C. The 6× His-tagged protein was purified from the supernatant by Ni-NTA affinity chromatography, followed by size-exclusion chromatography on a Superdex 200 HR 16/60 column on an ÄKTA FPLC system (GE Healthcare) equilibrated with size exclusion elution buffer [50 mM Hepes, 250 mM KCl, 1 mM $MgCl_2$, Triton X-100 0.002%, 0.5 mM TCEP, and 6% glycerol (pH 7.5)]. The eluted proteins were fractionated on SDS—polyacrylamide gel electrophoresis and stained with Coomassie Brilliant Blue dye (fig. S2C). For single-molecule motility experiments, full-length GFP- and 6× His-tagged Cin8 was overexpressed and purified from *S. cerevisiae* cells using Ni-NTA affinity and Superose 6 size exclusion columns, as previously described (*12, 54*).

Sample preparation for cryo-EM

The MT polymerization reaction mixture contained final concentrations of porcine tubulin (10 mg/ml; Cytoskeleton Inc.) and 1.5 mM GTP in general tubulin buffer (GTB; Cytoskeleton Inc.). The mixture was incubated for 50 min at 37°C, followed by the addition of Taxol (Sigma-Aldrich) to a final concentration of 100 μM, and another 20-min incubation at 37°C. After the polymerization of the MTs, the mixture was diluted ninefold with GTB supplemented with 10 μM Taxol (GTB-Tx), and centrifuged for 20 min at 15,000*g*. The supernatant was discarded, and the pellet was resuspended in 40 μl of GTB-Tx. A pre-reaction mixture was then prepared so as to provide final concentrations of 0.1 mM AMPPNP and 100 mM KCl in GTB-Tx. The $Cin8_{L8Kip1}$ construct was added in a ratio of 4:1 to the MTs (tubulin concentration of the MTs was ~0.13 mg/ml). The mixture was mixed gently and incubated for 10 min. Cryo-EM samples were prepared by plunge-freezing into liquid ethane. Thereafter, 3 μl of the mixture was applied onto glow-discharged Lacey F/C grids (01883-F), blotted for 20 s, and then vitrified by rapidly plunging into liquid ethane using an FEI Vitrobot operating at room temperature and 100% humidity. The frozen samples were stored in liquid nitrogen until imaging.

Cryo-EM data collection and structure determination

Samples were loaded under cryogenic conditions and imaged in low-dose mode on an FEI Tecnai F30 Polara microscope (FEI, Eindhoven) operated at 300 kV. Datasets were collected using SerialEM (*68*) and an in-house prepared semiautomated data collection script (*69*). Images were collected by a K2 Summit direct electron detector fitted behind an energy filter (Gatan Quantum GIF) set to ±10 eV around the zero-loss peak. The calibrated pixel size in the sample plane was 1.1 Å. The

detector was operated in a dose-fractionated counting mode at a dose rate of ~8 ē/pixel per second. Each dose-fractionated movie comprised 50 frames, with a total electron dose of 80 ē/Å^2. Data were collected at a defocus range of −1.0 to −2.0 μm (fig. S2, E and F).

Movies were motion-corrected using the MotionCor2 program (*70*) and contrast transfer function estimation was done with the ctffind4.1 program (*71*). All further processing was done on the motion-corrected micrographs. Particles were picked "start to end" manually with the RELION program (*72*). MT image segments from selected imaged filaments (approximately one per 8-nm repeat) were initially sorted on the basis of their symmetry type by using RELION 3D classification. Kinesin-decorated 12, 13, and 14 protofilament MT models synthetically generated from PDB models were used to seed the classification. Segments from the resulting 14 protofilament MT class were then subjected to 3D structure refinement using RELION with "asymmetric" helical repeats (14-fold tubular symmetry was not applied).

Additional "protofilament refinement" steps followed the scheme presented in (*73*). Refined MT segment alignment parameters were then "smoothed" to remove outliers and to fill in the gaps along the filament trajectories (*74*). Smoothed alignments were then 14-fold symmetrized to obtain coordinates and Euler angle particles corresponding to individual protofilaments. A wedge-shaped mask was then used to remove a single protofilament from the refined, 14-protofilament MT map. The resulting "13-protofilament" map was subtracted from the initial particle stack to generate a stack of protofilament particles. Additional rounds of RELION refinement were then performed using the wedge mask, and the resulting protofilament coordinates and 3D volume were used for a second round of subtraction: 13 individually aligned, projected protofilaments were subtracted from each segment to generate a stack of improved protofilament particles. This stack was then classified to determine the shift register of (i.e., to identify) the alternating α- and β-tubulin subunits within each protofilament. Shifts were then applied to protofilament coordinates to put all the protofilaments in the correct α/β register, and lastly, the protofilament particles were subjected to an additional round of 3D structure refinement with RELION. The nominal resolution of the resulting map (0.143 "gold standard") was 6.1 Å. An initial Cin8$_{L8Kip1}$ motor domain cryo-EM structure model, based on the crystal structure of Eg5 with AMPPNP as a nucleotide (PDB: 3HQD), was generated using SWISS-MODEL and fitted into the density map by manual real-space refinement using Coot v0.9. Figures of the maps and the fitted models were prepared using UCSF-Chimera (*75*). The cryo-EM map has been deposited in the EMDB (accession code EMD-10625).

Homology modeling

To determine the conformation of the NTnmd, homology modeling was performed. The outcome was then fitted to the experimental density map obtained by cryo-EM. Initially, the 3D structure of the human kinesin-like protein KIF2A [6BBN (*52*)] was used as a template to model the 3D structure of the kinesin-5 Cin8 (Cin8$_{L8Kip1}$ motor domain; amino acids 39 to 438). MODELLER v9.25 was used to build 1000 homology models of Cin8 (*76*), and the models were sorted according to a discrete optimized protein energy (DOPE-HR; using a bin size of 0.0125 nm) score. Thereafter, the modeled parts were fitted into the density seen in the cryo-EM, as described above.

Molecular dynamics

Simulation systems were prepared using the VMD package version 1.93 (*77*). The simulated protein was solvated in a water box with a minimum solvation shell of 15 Å thickness. Simulated systems were then neutralized by adding counter ions at random positions. Before initiating free molecular dynamics simulations, all systems were minimized and equilibrated. Initially, each system was submitted to 20K steps of conjugate gradient minimization in which the protein's heavy atoms were positionally restrained. This minimization was followed by two steps of equilibration. First, simulation systems were heated to 300 K while simulated for 200 ps under NVT conditions [moles (N) volume (V) and temperature (T) are kept constant] with the solute's heavy atoms restrained. Second, all systems were simulated using the NPT ensemble for 100 ns, while restraints were gradually removed. Last, each system was submitted to free NPT 200-ns length molecular dynamics simulations. Simulations were run in triplicate starting from different random seeds.

During the simulations, a time step of 2 fs was used. In all simulations, periodic boundary conditions with the PME algorithm for electrostatics were used (*78*). All simulations were performed at 300 K and 1 atm, using Langevin dynamics with a Langevin piston with a damping coefficient of 1 ps^{-1}, an oscillation period of 100 fs, and a decay time of 50 fs; switching and cutoff distances were 1 and 1.2 nm, respectively, and pair list distance was 1.4 nm.

All simulations were performed using the NAMD molecular dynamics simulation package version 2.13 (*78*) with CUDA extensions for accelerated calculation of long-range electrostatic potentials and nonbonded forces on graphics processing units (*79*). All structures were modeled with the CHARMM 36/CMAP force field (*80*), and water was explicitly represented by the TIP3P model (*81*).

Sequence alignments

All sequence alignments were calculated by the MUSCLE algorithm (*82*) and by the Jalview 2.11.1.0 program (*83*).

S. cerevisiae cell viability assay

Viability assays of cells expressing HA-tagged Cin8 variants as the sole source of kinesin-5 were performed as previously described (*13*, *29*). Briefly, the *S. cerevisiae* strains used for the assay were deleted of their chromosomal copies of *CIN8* and *KIP1* and contained an endogenic recessive cycloheximide-resistance gene (*cin8*Δ*kip1*Δ*cyh*^{r}), along with a plasmid (pMA1208) encoding for wt Cin8 and a wt dominant cycloheximide sensitivity gene (*CYH*). Following transformation with a plasmid encoding for a specific Cin8 variant, the pMA1208 plasmid was shuffled out by growth on yeast extract, peptone, and dextrose medium containing cycloheximide (7.5 μg/ml) at different temperatures. On plates containing cycloheximide, the shuffle plasmid was removed and only cells expressing functional Cin8 remained viable.

Live cell imaging

Live cells were imaged as previously described (*25*, *26*) using a *S. cerevisiae* strain deleted of the chromosomal copy of *CIN8* and endogenously expressing both the tdTomato-tagged SPB component Spc42 (strains listed in table S2), and 3GFP-tagged Cin8 variants under a Cin8 native promoter from a centromeric plasmid, listed in table S3. *S. cerevisiae* cells were grown overnight and diluted for 2 hours before imaging in a medium lacking tryptophan. Images of 15 Z-stack planes of live yeast cells placed on a low-fluorescence agarose gel at room temperature were acquired in three channels—bright field, green fluorescence, and red fluorescence, with a 0.5-μm separation between the planes. For each variant, three to four experiments were performed in which at least 200 cells were examined for each experiment.

For spindle length distribution in budded cells, as shown in Fig. 2, the distance between the two Spc42-tdTomato SPB components was measured on the projections of the Z-stacks. Accordingly, for each variant, budded cells were categorized into four categories: monopolar cells, short bipolar cells with a short <1.8-μm spindle, early anaphase cells with a spindle length of 1.8 to 4 μm, and late anaphase cells with a long spindle of length >4 μm. In addition, the budded cells were categorized into three phenotypes, according to Cin8 localization (as shown in Fig. 2) as normal, mislocalized, and no Cin8 signal, except in the anaphase stages, where Cin8 normally has a diffusive/mislocalized localization. Cells with monopolar spindles were defined as budded cells with a single Spc42-tdTomato SPB signal in the mother cell. The percentage of budded cells in each category was averaged for three experiments for each variant. For each variant, three to four experiments were performed in which at least 200 cells were examined for each experiment. Statistical analysis was performed by one-way analysis of variance (ANOVA), followed by Dunnett's analysis (*84*), compared to wt Cin8 in each spindle length category; degrees of freedom = 12, and *F* factors 2.90 ($\alpha = 0.05$) and 3.81 ($\alpha = 0.01$).

Single-molecule motility assay

This assay was performed as previously described (*12, 54*), using commercially available tubulin (Cytoskeleton Inc., USA). Briefly, GMPCPP-stabilized, fluorescently labeled, biotinylated MTs were polymerized with tubulin (1 mg/ml), biotinylated tubulin (0.08 mg/ml), and rhodamine-labeled tubulin (0.08 mg/ml), in the presence of 1 mM GMPCPP for 1 hour at 37°C in GTB [80 mM Pipes, 0.5 mM EGTA, and 2 mM $MgCl_2$ (pH 6.9)]. For plus-end polarity labeling, additional rhodamine-labeled tubulin at a concentration of 0.1 mg/ml was added to the polymerized MTs, and the mixture was further incubated for 45 min at 37°C. After polymerization, the mixture was diluted 10-fold in GTB containing 20 μM Taxol and centrifuged for 15 min at 17,000*g*. The supernatant was discarded, and the MT pellet was resuspended in 50 μl of GTB with 20 μM Taxol and stored at 28°C. To prepare subtilisin-treated MTs (*17*, *18*), the MTs were stabilized after polymerization with 20 μM Taxol and then exposed to subtilisin (400 μg/ml) for 30 min at 37°C; thereafter, proteolysis was inactivated with 10 mM phenylmethylsulfonyl fluoride. The workup for the resulting mixture was then continued in the same way as that for the nontreated MTs. Coverslips, silanized with 0.1% dimethyldichlorosilane in trichloroethylene and assembled into flow cells, were coated with biotinylated bovine serum albumin (Sigma-Aldrich) and then with NeutrAvidin (Life Technologies). Following the attachment of the biotinylated MTs to the coverslips through biotin-NeutrAvidin interaction, 20 μl of the GFP-labeled Cin8 N-terminal variant in motility buffer [50 mM tris-HCl, 30 mM Pipes, 110 mM KCl, 2 mM $MgCl_2$, 1 mM EGTA, casein (50 μg/ml), 1 mM dithiothreitol, 1 mM ATP, 10 mM glucose, glucose oxidase (100 μg/ml), catalase (80 μg/ml), 10 mM phosphocreatine, and creatine kinase (50 μg/ml) (pH 7.2)] was perfused into the flow cell. For the Cin8 inhibition assay, STLC stock solution at 50 mM in 100% Me_2SO was prepared and subsequently diluted in Me_2SO before addition to the motility buffer so as to maintain a constant Me_2SO concentration of 2%. Motility without STLC but in the presence of 2% Me_2SO was also investigated to ascertain any Me_2SO inhibition effect. For Cin8-GFP motility and photobleaching experiments, 90 images were acquired at 1 fps with an exposure time of 800 ms. All data were acquired in at least three independent experiments.

MT sliding assay

MT sliding assay was performed on piranha-cleaned salinized coverslips as previously described (*29*). MTs were polymerized using commercially available tubulin (Cytoskeleton Inc.) with bright seeds at their plus-ends, with and without biotinylated tubulin. Biotinylated MTs were first adhered to the coverslips via biotin-NeutrAvidin interaction, and then Cin8 was added in motility buffer containing 120 mM KCl supplemented with 5 μM Taxol, followed by a ~4-min incubation of immobilized MTs with Cin8. Then, free MTs (polymerized without biotinylated tubulin) were added to the motility buffer, as above, and incubated for an additional ~4 min before imaging. Time-lapse imaging for 300 s with 1-s exposure and 10-s intervals was then acquired. Motor concentration was in the range of 0.08 to 0.28 mg/ml, adjusted such that sufficient MT sliding events could be observed without extensive MT bundling. The velocity of the moving MTs was calculated by dividing the distance of displacement on the MT by the corresponding time. The directionality of sliding was classified according to the plus-end labeling of the stationary and sliding MTs. Bidirectional sliding was assigned when both plus- and minus-end–directed sliding of free MTs along stationary MTs was observed in the same 300-s time-lapse sequence. Statistical analysis of sliding velocities compared to antiparallel plus-end–directed sliding of wt Cin8 was calculated by ANOVA followed by Tukey's test (*85*).

Imaging

Imaging was performed using a wide-field illumination Micro-Manager controlled Zeiss Axiovert 200M microscope equipped with a cooled CCD Andor Neo sCMOS camera and a Plan-Apochromat DIC 100×/1.4NA objective (pixel size: 124 nm). Filter sets (Chroma) #49002, ET-eGFP (FITC/Cy2) [for GFP] and #49004: ET-CY3/TRITC [for rhodamine and tdTomato] were used for imaging Cin8-GFP, rhodamine-MTs, and tdTomato-tagged SPB, respectively.

Single-molecule motility and MT binding analyses

MT polarity was assigned based on bright plus-end labeling (*12*). Image analysis and kymographs were conducted with ImageJ-Fiji software (*86*). The *x-y* coordinates of motile GFP-labeled motors for MD analysis from the obtained kymographs were determined with the Kymobutler program (*87*). MD analysis was performed as previously described (*13, 29, 54*). The MD values for all possible time intervals (T) were calculated by averaging each time interval displacement, calculated for all motility recordings of Cin8-GFP on the MTs. Average velocities (*V*) were derived from the linear MD fit, MD = *V*·T.

The sorting of Cin8 motors into single molecules and clusters was performed as previously described (*13, 29, 53, 54*). Our examination of the fluorescence intensity of fluorescent Cin8 molecules as a function of time showed that the intensity was bleached in steps of ~50 a.u., with each step representing the photobleaching of 1 GFP. Since Cin8 is a homotetrameric motor and one GFP is attached to each subunit chain, the Cin8 tetramer (referred to as a single Cin8 molecule in this article) contains four GFPs. Hence, all Cin8 motors having an intensity ≤200 a.u. were likely to be single tetrameric Cin8 molecules. To minimize the effect of GFP photobleaching on the determination of the Cin8 cluster size, all motility measurements were performed only on those Cin8 motors that started moving within the first 30 s of each measurement. In addition, the Cin8-GFP fluorescence intensity was measured only in the first frame of its appearance, thereby reducing the likelihood of estimating the cluster size of a photobleached motor. Using this method, we assigned

intensity ranges of Cin8-GFP fluorescence as ≤200 and >200 a.u. for single Cin8 molecules and Cin8 clusters, respectively.

Binding to MTs by the different Cin8 variants was quantitatively determined as previously described (*13*, *29*). The total number of MT-bound motors was divided by the total MT length in fields of 500 μm^2. The average number of MT-bound motors per MT length (±SEM) was determined in a number of fields, as indicated in Fig. 7B.

Supplementary Materials

This PDF file includes:
Figs. S1 to S7
Tables S1 to S3
Legend for movies S1 to S4

Other Supplementary Material for this manuscript includes the following:
Movies S1 to S4

REFERENCES AND NOTES

1. H. Pandey, M. Popov, A. Goldstein-Levitin, L. Gheber, Mechanisms by which kinesin-5 motors perform their multiple intracellular functions. *Int. J. Mol. Sci.* **22**, 6420 (2021).
2. B. J. Mann, P. Wadsworth, Kinesin-5 regulation and function in mitosis. *Trends Cell Biol.* **29**, 66–79 (2019).
3. S. K. Singh, H. Pandey, J. Al-Bassam, L. Gheber, Bidirectional motility of kinesin-5 motor proteins: Structural determinants, cumulative functions and physiological roles. *Cell. Mol. Life Sci.* **75**, 1757–1771 (2018).
4. A. Goulet, C. Moores, New insights into the mechanism of force generation by kinesin-5 molecular motors. *Int. Rev. Cell Mol. Biol.* **304**, 419–466 (2013).
5. J. E. Scholey, S. Nithianantham, J. M. Scholey, J. Al-Bassam, Structural basis for the assembly of the mitotic motor kinesin-5 into bipolar tetramers. *eLife* **3**, e02217 (2014).
6. S. Acar, D. B. Carlson, M. S. Budamagunta, V. Yarov-Yarovoy, J. J. Correia, M. R. Ninonuevo, W. Jia, L. Tao, J. A. Leary, J. C. Voss, J. E. Evans, J. M. Scholey, The bipolar assembly domain of the mitotic motor kinesin-5. *Nat. Commun.* **4**, 1343 (2013).
7. A. S. Kashina, R. J. Baskin, D. G. Cole, K. P. Wedaman, W. M. Saxton, J. M. Scholey, A bipolar kinesin. *Nature* **379**, 270–272 (1996).
8. M. Edamatsu, Bidirectional motility of the fission yeast kinesin-5, Cut7. *Biochem. Biophys. Res. Commun.* **446**, 231–234 (2014).
9. V. Fridman, A. Gerson-Gurwitz, O. Shapira, N. Movshovich, S. Lakamper, C. F. Schmidt, L. Gheber, Kinesin-5 Kip1 is a bi-directional motor that stabilizes microtubules and tracks their plus-ends in vivo. *J. Cell Sci.* **126**, 4147–4159 (2013).
10. J. Roostalu, C. Hentrich, P. Bieling, I. A. Telley, E. Schiebel, T. Surrey, Directional switching of the kinesin Cin8 through motor coupling. *Science* **332**, 94–99 (2011).
11. A. Gerson-Gurwitz, C. Thiede, N. Movshovich, V. Fridman, M. Podolskaya, T. Danieli, S. Lakamper, D. R. Klopfenstein, C. F. Schmidt, L. Gheber, Directionality of individual kinesin-5 Cin8 motors is modulated by loop 8, ionic strength and microtubule geometry. *EMBO J.* **30**, 4942–4954 (2011).
12. O. Shapira, A. Goldstein, J. Al-Bassam, L. Gheber, A potential physiological role for bi-directional motility and motor clustering of mitotic kinesin-5 Cin8 in yeast mitosis. *J. Cell Sci.* **130**, 725–734 (2017).
13. H. Pandey, S. K. Singh, M. Sadan, M. Popov, M. Singh, G. Davidov, S. Inagaki, J. Al-Bassam, R. Zarivach, S. S. Rosenfeld, L. Gheber, Flexible microtubule anchoring modulates the bi-directional motility of the kinesin-5 Cin8. *Cell. Mol. Life Sci.* **78**, 6051–6068 (2021).
14. A. Duselder, V. Fridman, C. Thiede, A. Wiesbaum, A. Goldstein, D. R. Klopfenstein, O. Zaitseva, M. E. Janson, L. Gheber, C. F. Schmidt, Deletion of the tail domain of the kinesin-5 Cin8 affects its directionality. *J. Biol. Chem.* **19**, 620799 (2015).
15. M. Britto, A. Goulet, S. Rizvi, O. von Loeffelholz, C. A. Moores, R. A. Cross, Schizosaccharomyces pombe kinesin-5 switches direction using a steric blocking mechanism. *Proc. Natl. Acad. Sci. U.S.A.* **113**, E7483–E7489 (2016).
16. R. Blackwell, C. Edelmaier, O. Sweezy-Schindler, A. Lamson, Z. R. Gergely, E. O'Toole, A. Crapo, L. E. Hough, J. R. McIntosh, M. A. Glaser, M. D. Betterton, Physical determinants of bipolar mitotic spindle assembly and stability in fission yeast. *Sci. Adv.* **3**, e1601603 (2017).
17. L. Serrano, J. de la Torre, R. B. Maccioni, J. Avila, Involvement of the carboxyl-terminal domain of tubulin in the regulation of its assembly. *Proc. Natl. Acad. Sci. U.S.A.* **81**, 5989–5993 (1984).
18. L. Serrano, J. Avila, R. B. Maccioni, Controlled proteolysis of tubulin by subtilisin: Localization of the site for MAP2 interaction. *Biochemistry* **23**, 4675–4681 (1984).
19. W. Hwang, M. J. Lang, M. Karplus, Force generation in kinesin hinges on cover-neck bundle formation. *Structure* **16**, 62–71 (2008).
20. A. S. Khalil, D. C. Appleyard, A. K. Labno, A. Georges, M. Karplus, A. M. Belcher, W. Hwang, M. J. Lang, Kinesin's cover-neck bundle folds forward to generate force. *Proc. Natl. Acad. Sci.* **105**, 19247–19252 (2008).
21. Y.-Z. Geng, T. Li, Q. Ji, S. Yan, Simulation study of interactions between kinesin's neck linker and motor domain. *Cell. Molec. Bioeng.* **7**, 99–105 (2014).
22. G. Yi-Zhao, J. Qing, L. Shu-Xia, Y. Shi-Wei, Initial conformation of kinesin's neck linker. *Chin. Phys. B* **23**, 108701 (2014).
23. B. G. Budaitis, S. Jariwala, D. N. Reinemann, K. I. Schimert, G. Scarabelli, B. J. Grant, D. Sept, M. J. Lang, K. J. Verhey, Neck linker docking is critical for Kinesin-1 force generation in cells but at a cost to motor speed and processivity. *eLife* **14**, 44146 (2019).
24. A. Goulet, J. Major, Y. Jun, S. P. Gross, S. S. Rosenfeld, C. A. Moores, Comprehensive structural model of the mechanochemical cycle of a mitotic motor highlights molecular adaptations in the kinesin family. *Proc. Natl. Acad. Sci. U.S.A.* **111**, 1837–1842 (2014).
25. A. Goldstein, D. Goldman, E. Valk, M. Loog, L. J. Holt, L. Gheber, Synthetic-evolution reveals narrow paths to regulation of the *Saccharomyces cerevisiae* mitotic kinesin-5 Cin8. *Int. J. Biol. Sci.* **15**, 1125–1138 (2019).
26. A. Goldstein, N. Siegler, D. Goldman, H. Judah, E. Valk, M. Koivomagi, M. Loog, L. Gheber, Three Cdk1 sites in the kinesin-5 Cin8 catalytic domain coordinate motor localization and activity during anaphase. *Cell. Mol. Life Sci.* **74**, 3395–3412 (2017).
27. R. Avunie-Masala, N. Movshovich, Y. Nissenkorn, A. Gerson-Gurwitz, V. Fridman, M. Koivomagi, M. Loog, M. A. Hoyt, A. Zaritsky, L. Gheber, Phospho-regulation of kinesin-5 during anaphase spindle elongation. *J. Cell Sci.* **124**, 873–878 (2011).
28. E. R. Hildebrandt, L. Gheber, T. Kingsbury, M. A. Hoyt, Homotetrameric form of Cin8p, a *Saccharomyces cerevisiae* kinesin-5 motor, is essential for its in vivo function. *J. Biol. Chem.* **281**, 26004–26013 (2006).
29. A. Goldstein-Levitin, H. Pandey, K. Allhuzaeel, I. Kass, L. Gheber, Intracellular functions and motile properties of bi-directional kinesin-5 Cin8 are regulated by neck linker docking. *eLife* **10**, e71036 (2021).
30. K. M. Bell, H. K. Cha, C. V. Sindelar, J. C. Cochran, The yeast kinesin-5 Cin8 interacts with the microtubule in a noncanonical manner. *J. Biol. Chem.* **12**, 797662 (2017).
31. M. A. Hoyt, L. He, K. K. Loo, W. S. Saunders, Two *Saccharomyces cerevisiae* kinesin-related gene products required for mitotic spindle assembly. *J. Cell Biol.* **118**, 109–120 (1992).
32. M. Dai, Z. Dong, K. Xu, Q. C. Zhang, CryoRes: Local resolution estimation of cryo-EM density maps by deep learning. *J. Mol. Biol.* **435**, 168059 (2023).
33. J. Turner, R. Anderson, J. Guo, C. Beraud, R. Fletterick, R. Sakowicz, Crystal structure of the mitotic spindle kinesin Eg5 reveals a novel conformation of the neck-linker. *J. Biol. Chem.* **276**, 25496–25502 (2001).
34. R. D. Vale, T. Funatsu, D. W. Pierce, L. Romberg, Y. Harada, T. Yanagida, Direct observation of single kinesin molecules moving along microtubules. *Nature* **380**, 451–453 (1996).
35. E. P. Sablin, F. J. Kull, R. Cooke, R. D. Vale, R. J. Fletterick, Crystal structure of the motor domain of the kinesin-related motor ncd. *Nature* **380**, 555–559 (1996).
36. C. L. Parke, E. J. Wojcik, S. Kim, D. K. Worthylake, ATP hydrolysis in Eg5 kinesin involves a catalytic two-water mechanism. *J. Biol. Chem.* **285**, 5859–5867 (2010).
37. O. von Loeffelholz, A. Pena, D. R. Drummond, R. Cross, C. A. Moores, Cryo-EM structure (4.5-A) of yeast kinesin-5-microtubule complex reveals a distinct binding footprint and mechanism of drug resistance. *J. Molec. Biol.* **431**, 864–872 (2019).
38. Z. Shang, K. Zhou, C. Xu, R. Csencsits, J. C. Cochran, C. V. Sindelar, High-resolution structures of kinesin on microtubules provide a basis for nucleotide-gated force-generation. *eLife* **3**, e04686 (2014).
39. C. V. Sindelar, A seesaw model for intermolecular gating in the kinesin motor protein. *Biophys. Rev.* **3**, 85–100 (2011).
40. C. V. Sindelar, K. H. Downing, An atomic-level mechanism for activation of the kinesin molecular motors. *Proc. Natl. Acad. Sci. U.S.A.* **107**, 4111–4116 (2010).
41. F. J. Kull, E. P. Sablin, R. Lau, R. J. Fletterick, R. D. Vale, Crystal structure of the kinesin motor domain reveals a structural similarity to myosin. *Nature* **380**, 550–555 (1996).
42. W. M. Behnke-Parks, J. Vendome, B. Honig, Z. Maliga, C. Moores, S. S. Rosenfeld, Loop L5 acts as a conformational latch in the mitotic kinesin Eg5. *J. Biol. Chem.* **286**, 5242–5253 (2011).
43. J. S. Waitzman, A. G. Larson, J. C. Cochran, N. Naber, R. Cooke, F. Jon Kull, E. Pate, S. E. Rice, The loop 5 element structurally and kinetically coordinates dimers of the human kinesin-5, Eg5. *Biophys. J.* **101**, 2760–2769 (2011).
44. A. G. Larson, N. Naber, R. Cooke, E. Pate, S. E. Rice, The conserved L5 loop establishes the pre-powerstroke conformation of the Kinesin-5 motor, eg5. *Biophys. J.* **98**, 2619–2627 (2010).
45. J. M. Muretta, Y. Jun, S. P. Gross, J. Major, D. D. Thomas, S. S. Rosenfeld, The structural kinetics of switch-1 and the neck linker explain the functions of kinesin-1 and Eg5. *Proc. Natl. Acad. Sci. U.S.A.* **112**, E6606–E6613 (2015).
46. J. M. Muretta, W. M. Behnke-Parks, J. Major, K. J. Petersen, A. Goulet, C. A. Moores, D. D. Thomas, S. S. Rosenfeld, Loop L5 assumes three distinct orientations during the ATPase cycle of the mitotic kinesin Eg5: A transient and time-resolved fluorescence study. *J. Biol. Chem.* **288**, 34839–34849 (2013).

47. A. Goulet, W. M. Behnke-Parks, C. V. Sindelar, J. Major, S. S. Rosenfeld, C. A. Moores, The structural basis of force generation by the mitotic motor kinesin-5. *J. Biol. Chem.* **287**, 44654–44666 (2012).
48. H. Asraf, R. Avunie-Masala, M. Hershfinkel, L. Gheber, Mitotic slippage and expression of survivin are linked to differential sensitivity of human cancer cell-lines to the Kinesin-5 inhibitor monastrol. *PLOS ONE* **10**, e0129255 (2015).
49. O. Rath, F. Kozielski, Kinesins and cancer. *Nat. Rev. Cancer* **12**, 527–539 (2012).
50. Z. Maliga, T. J. Mitchison, Small-molecule and mutational analysis of allosteric Eg5 inhibition by monastrol. *BMC Chem. Biol.* **6**, 2 (2006).
51. I. Leizerman, R. Avunie-Masala, M. Elkabets, A. Fich, L. Gheber, Differential effects of monastrol in two human cell lines. *Cell. Mol. Life Sci.* **61**, 2060–2070 (2004).
52. D. Trofimova, M. Paydar, A. Zara, L. Talje, B. H. Kwok, J. S. Allingham, Ternary complex of Kif2A-bound tandem tubulin heterodimers represents a kinesin-13-mediated microtubule depolymerization reaction intermediate. *Nat. Commun.* **9**, 2628 (2018).
53. H. Pandey, T. Zvagelsky, M. Popov, M. Sadan, N. Yanir, A. Goldstein-Levitin, N. Siegler, S. Hershfinkel, Y. Abraham, R. Abraham, L. A. Gheber, L. Gheber, Motility of single molecules and clusters of bi-directional kinesin-5 Cin8 purified from *S. cerevisiae* cells. *J. Vis. Exp.* **2**, 63425 (2022).
54. H. Pandey, E. Reithmann, A. Goldstein-Levitin, J. Al-Bassam, E. Frey, L. Gheber, Drag-induced directionality switching of kinesin-5 Cin8 revealed by cluster-motility analysis. *Sci. Adv.* **7**, eabc1687 (2021).
55. O. Shapira, L. Gheber, Motile properties of the bi-directional kinesin-5 Cin8 are affected by phosphorylation in its motor domain. *Sci Rep-Uk* **6**, 25597 (2016).
56. Y. C. Zhao, F. J. Kull, J. C. Cochran, Modulation of the kinesin ATPase cycle by neck linker docking and microtubule binding. *J. Biol. Chem.* **285**, 25213–25220 (2010).
57. T. Bodrug, E. M. Wilson-Kubalek, S. Nithianantham, A. F. Thompson, A. Alfieri, I. Gaska, J. Major, G. Debs, S. Inagaki, P. Gutierrez, L. Gheber, R. J. McKenney, C. V. Sindelar, R. Milligan, J. Stumpff, S. S. Rosenfeld, S. T. Forth, J. Al-Bassam, The kinesin-5 tail domain directly modulates the mechanochemical cycle of the motor domain for anti-parallel microtubule sliding. *eLife* **9**, 51131 (2020).
58. M. Matsushita, K. Y. Fau-Mitsui, H. M. Fau-Kanazawa, H. Kanazawa, Altered motor activity of alternative splice variants of the mammalian kinesin-3 protein KIF1B. *Traffic* **10**, 1647–1654 (2009).
59. B. G. Budaitis, S. Jariwala, L. Rao, Y. Yue, D. Sept, K. J. Verhey, A. Gennerich, Pathogenic mutations in the kinesin-3 motor KIF1A diminish force generation and movement through allosteric mechanisms. *J. Cell Biol.* **220**, e202004227 (2021).
60. V. Soppina, K. J. Verhey, The family-specific K-loop influences the microtubule on-rate but not the superprocessivity of kinesin-3 motors. *Mol. Biol. Cell* **25**, 2161–2170 (2014).
61. A. J. Lam, L. Rao, Y. Anazawa, K. Okada, K. Chiba, M. Dacy, S. Niwa, A. Gennerich, D. W. Nowakowski, R. J. McKenney, A highly conserved 3_{10} helix within the kinesin motor domain is critical for kinesin function and human health. *Sci. Adv.* **7**, eabf1002 (2021).
62. D. V. Lessard, O. J. Zinder, T. Hotta, K. J. Verhey, R. Ohi, C. L. Berger, Polyglutamylation of tubulin's C-terminal tail controls pausing and motility of kinesin-3 family member KIF1A. *J. Biol. Chem.* **294**, 6353–6363 (2019).
63. S. M. Block, Kinesin motor mechanics: Binding, stepping, tracking, gating, and limping. *Biophys. J.* **92**, 2986–2995 (2007).
64. B. E. Clancy, W. M. Behnke-Parks, J. O. Andreasson, S. S. Rosenfeld, S. M. Block, A universal pathway for kinesin stepping. *Nat. Struct. Mol. Biol.* **18**, 1020–1027 (2011).
65. S. Shastry, W. O. Hancock, Interhead tension determines processivity across diverse N-terminal kinesins. *Proc. Natl. Acad. Sci. U.S.A.* **108**, 16253–16258 (2011).
66. S. Shastry, W. O. Hancock, Neck linker length determines the degree of processivity in kinesin-1 and kinesin-2 motors. *Curr. Biol.* **20**, 939–943 (2010).
67. A. Yildiz, M. Tomishige, A. Gennerich, R. D. Vale, Intramolecular strain coordinates kinesin stepping behavior along microtubules. *Cell* **134**, 1030–1041 (2008).
68. D. N. Mastronarde, Automated electron microscope tomography using robust prediction of specimen movements. *J. Struct. Biol.* **152**, 36–51 (2005).
69. G. Davidov, G. Abelya, R. Zalk, B. Izbicki, S. Shaibi, L. Spektor, D. Shagidov, E. G. Meyron-Holtz, R. Zarivach, G. A. Frank, Folding of an intrinsically disordered iron-binding peptide in response to sedimentation revealed by Cryo-EM. *J. Am. Chem. Soc.* **142**, 19551–19557 (2020).
70. S. Q. Zheng, E. Palovcak, J. P. Armache, K. A. Verba, Y. Cheng, D. A. Agard, MotionCor2: Anisotropic correction of beam-induced motion for improved cryo-electron microscopy. *Nat. Methods* **14**, 331–332 (2017).
71. A. Rohou, N. Grigorieff, CTFFIND4: Fast and accurate defocus estimation from electron micrographs. *J. Struct. Biol.* **192**, 216–221 (2015).
72. S. He, S. H. W. Scheres, Helical reconstruction in RELION. *J. Struct. Biol.* **198**, 163–176 (2017).
73. G. E. Debs, M. Cha, X. Liu, A. R. Huehn, C. V. Sindelar, Dynamic and asymmetric fluctuations in the microtubule wall captured by high-resolution cryoelectron microscopy. *Proc. Natl. Acad. Sci. U.S.A.* **117**, 16976–16984 (2020).
74. D. Liu, X. Liu, Z. Shang, C. V. Sindelar, Structural basis of cooperativity in kinesin revealed by 3D reconstruction of a two-head-bound state on microtubules. *eLife* **6**, 24490 (2017).
75. E. F. Pettersen, T. D. Goddard, C. C. Huang, G. S. Couch, D. M. Greenblatt, E. C. Meng, T. E. Ferrin, UCSF Chimera—A visualization system for exploratory research and analysis. *J. Comput. Chem.* **25**, 1605–1612 (2004).
76. B. Webb, A. Sali, comparative protein structure modeling using MODELLER. *Curr. Protoc. Bioinformatics* **54**, 5.6.1–5.6.37 (2016).
77. W. Humphrey, A. Dalke, K. Schulten, VMD: Visual molecular dynamics. *J. Mol. Graph.* **14**, 27–38 (1996).
78. U. Essmann, L. Perera, M. L. Berkowitz, T. Darden, H. Lee, L. G. Pedersen, A smooth particle mesh Ewald method. *J. Chem. Phys.* **103**, 8577–8593 (1995).
79. J. C. Phillips, R. Braun, W. Wang, J. Gumbart, E. Tajkhorshid, E. Villa, C. Chipot, R. D. Skeel, L. Kalé, K. Schulten, Scalable molecular dynamics with NAMD. *J. Comput. Chem.* **26**, 1781–1802 (2005).
80. R. B. Best, X. Zhu, J. Shim, P. E. Lopes, J. Mittal, M. Feig, A. D. Mackerell Jr., Optimization of the additive CHARMM all-atom protein force field targeting improved sampling of the backbone φ, ψ and side-chain $\chi(1)$ and $\chi(2)$ dihedral angles. *J. Chem. Theory. Comput.* **8**, 3257–3273 (2012).
81. W. L. Jorgensen, J. Chandrasekhar, J. D. Madura, R. W. Impey, M. L. Klein, Comparison of simple potential functions for simulating liquid water. *J. Chem. Phys.* **79**, 926–935 (1983).
82. R. C. Edgar, MUSCLE: A multiple sequence alignment method with reduced time and space complexity. *BMC Bioinformatics* **5**, 113 (2004).
83. A. M. Waterhouse, J. B. Procter, D. M. Martin, M. Clamp, G. J. Barton, Jalview Version 2—A multiple sequence alignment editor and analysis workbench. *Bioinformatics* **25**, 1189–1191 (2009).
84. C. W. Dunnett, A multiple comparison procedure for comparing several treatments with a control. *J. Am. Stat. Assoc.* **50**, 1096–1121 (1955).
85. J. W. Tukey, Comparing individual means in the analysis of variance. *Biometrics* **5**, 99–114 (1949).
86. J. Schindelin, I. Arganda-Carreras, E. Frise, V. Kaynig, M. Longair, T. Pietzsch, S. Preibisch, C. Rueden, S. Saalfeld, B. Schmid, J. Y. Tinevez, D. J. White, V. Hartenstein, K. Eliceiri, P. Tomancak, A. Cardona, Fiji: An open-source platform for biological-image analysis. *Nat. Methods* **9**, 676–682 (2012).
87. M. A. H. Jakobs, A. Dimitracopoulos, K. Franze, KymoButler, a deep learning software for automated kymograph analysis. *eLife* **8**, e42288 (2019).

Acknowledgments: We thank S. Hershfinkel from the L.G. laboratory for purifying the full-length Cin8 variants used in the in vitro experiments with subtilisin-treated MTs (Figs. 6 and 7). **Funding:** This work was supported in part by the Israel Science Foundation (ISF) Grants #286-18 and #629-23 and the U.S.-Israel Binational Research Foundation (BSF) Grant #2019008, awarded to L.G. C.V.S. and G.D. were supported by the National Institute of General Medical Sciences of the NIH under award number R01GM110530. **Author contributions:** Conceptualization: S.K.S., N.S., H.P., A.G.-L., R.Zal., and L.G. Funding acquisition: C.V.S. and L.G. Project administration: C.V.S. and L.G. Supervision: S.K.S., H.P., A.G.-L., C.V.S., and L.G. Investigation: S.K.S., N.S., H.P., N.Y., M.P., A.G.-L., M.S., R.Zar., I.K., R.Zal., and L.G. Validation: S.K.S., H.P., N.S., N.Y., M.P., A.G.-L., M.S., I.K., G.A.F., C.V.S., R.Zal., and L.G. Formal analysis: S.K.S., N.S., H.P., N.Y., M.P., A.G.-L., M.S., I.K., C.V.S., R.Zal., and L.G. Visualization: S.K.S., H.P., N.S., N.Y., M.P., A.G.-L., I.K., R.Zal., and L.G. Data curation: S.K.S., H.P., N.S., A.G.-L., I.K., C.V.S., R.Zal., and L.G. Resources: S.K.S., H.P., N.S., G.A.F., C.V.S., R.Zal., and L.G. Methodology: S.K.S., N.S., H.P., G.D., R.Zar., G.A.F., I.K., C.V.S., R.Zal., and L.G. Software: G.D., I.K., G.A.F., and C.V.S. Writing—original draft: S.K.S., N.S., H.P., N.Y., R.Zar., I.K., R.Zal., and L.G. Writing—review and editing: S.K.S., H.P., N.S., A.G.-L., M.S., I.K., R.Zal., and L.G. **Competing interests:** The authors declare that they have no competing interests. **Data and materials availability:** All data needed to evaluate the conclusions in the paper are present in the paper and/or the Supplementary Materials. The cryo-EM map has been deposited in the EMDB (accession code: EMD-10625).

Submitted 13 April 2023
Accepted 8 January 2024
Published 7 February 2024
10.1126/sciadv.adi1367